Cyclic Behavior of T-Shaped Composite Plate Shear Walls–Concrete Filled

Emre Kizilarslan, Ph.D., S.M.ASCE[1]; and Michel Bruneau, Ph.D., P.Eng., Dist.M.ASCE[2]

Abstract: This paper presents findings from experiments conducted on four large-scale T-shaped concrete filled composite plate shear walls (C-PSW/CF) specimens subjected to axial force and flexure. A C-PSW/CF is a *sandwich* type of construction by which concrete (without rebars) is enclosed between steel plates connected by tie bars. One of the walls was subjected to a cyclic wind loading protocol and the other walls were cycled with a seismic loading protocol. Their dimensions were identical, but different axial loads (up to 30% of the crushing load of the infill concrete, $A_c f'_c$) were applied. The plastic hinge development was investigated along with the composite behavior and compared with the calculated plastic moment of the corresponding cross section. These tests along with the results on C-shaped wall tests were conducted to establish the development of design guidelines for high-rise core-wall steel buildings having C-PSW/CF as the primary lateral force resisting system. **DOI: 10.1061/JSENDH.STENG-11693.**

Author keywords: Composite plate shear walls; Cyclic testing; Inelastic behavior; Flexural behavior; Ductility; Plate buckling; Fracture; Strength degradation.

Introduction and Background

A composite plate shear wall/concrete filled (C-PSW/CF) is a *sandwich* type of construction by which concrete (without rebars) is enclosed between steel plates connected by tie bars (Fig. 1). As a lateral load resisting system, these walls have advantages over typical reinforced concrete walls due to their relatively high shear strength, deformation capacity, and rapid on-site construction.

Similar walls with various details have been used in the past for different applications, with different names, sometimes referred to as steel-plate composite (SC) wall, steel/concrete/steel sandwich construction, double skin composite walls, or Bi-Steel, among many names used. Here, SC is used to generically refer to the past research for multiple applications, whereas C-PSW/CF refers to the North American type walls detailed per the AISC-341 (AISC 2016) seismic requirements. Past experimental research on SC walls was generally carried out on modest size scaled specimens and focused predominantly on the elastic range of response. Some of the work that investigated the performance of SC walls for offshore structures and blast resistant facilities (such as nuclear power plants) addressed inelastic response. For example, Adams et al. (1987), Gerwick and Berner (1987), Matsuishi and Iwata (1987), O'Flynn and MacGregor (1988), and Smith and McLeish (1987) used composite steel/concrete walls to armor arctic oil and gas production structures against large and concentrated ice forces and experimentally demonstrated high out-of-plane strength and ductility. Later, Wright (1998) tested twenty composite shear walls made of corrugated steel web plates and infill concrete under combination of axial and in-plane bending loads, but full plastic flexural strength of the specimens was not achieved because the test specimens had no shear connectors (such as tie bars or studs). Others showed that these composite walls could also be suitable as deep beams, devices producing energy from waves, and blast resistant walls (Bruhl and Varma 2018; Liew and Wang 2011).

SC walls were intended to be used as an alternative to conventional reinforced concrete (RC) walls in nuclear facilities, due to their economic and structural efficiency. For the past 30 years, researchers in Korea, Japan, and the United States have investigated applications of steel plate composite (SC) walls in nuclear safety structures. (e.g., Akita et al. 2001; Akiyama et al. 1989; Ozaki et al. 2004; Sasaki et al. 1995; Takeuchi et al. 1995). Japanese and Koreans were the first to develop design codes for SC walls [JEAG 4618 (JEA 2005)]. The US followed, by implementing provisions in AISC N690 (AISC 2014) building from the Japanese and Korean practice and the work of Bhardwaj and Varma (2017) and Varma et al. (2014).

For buildings, referring to the SC walls as "Bi-Steel," Bowerman and Chapman (2002) and Bowerman et al. (1999) provided a design guide for their use in mid-rise construction in nonseismic regions. However, for implementation as a lateral load resisting system of buildings in seismic regions, knowledge was needed on in-plane flexural hysteretic response. Eom et al. (2009) tested single walls and coupled walls but observed premature fractures of the welded connections at the wall base before some of walls reached their load carrying capacity due to poor connection detailing. Moreover, these tests were conducted without concurrent axial loading. Ramesh (2013) also investigated the cyclic behavior of a cantilever T-shaped wall. During testing, buckling was observed relatively early in the steel plates at the end of web, at approximately 0.75% drift, and the specimen could not reach the target of 2% drift in the negative direction (also in part due to tie failures). Epackachi et al. (2015) tested four rectangular squat walls (height-to-length ratio of 1.0) to investigate their inelastic cyclic lateral load response, but since the ends of the walls were left open, severe buckling and rupture of the steel face plates occurred there together with crushing of the concrete, which resulted in a rapid drop of strength after peak strength.

[1]Graduate Research Assistant, Dept. of Civil Structural and Environmental Engineering, Univ. at Buffalo, Buffalo, NY 14260 (corresponding author). ORCID: https://orcid.org/0000-0003-3014-1165. Email: emrekizilarslan91@gmail.com

[2]Professor, Dept. of Civil Structural and Environmental Engineering, Univ. at Buffalo, Buffalo, NY 14260. ORCID: https://orcid.org/0000-0003-1170-468X. Email: bruneau@buffalo.edu

Note. This manuscript was submitted on May 25, 2022; approved on March 30, 2023; published online on May 27, 2023. Discussion period open until October 27, 2023; separate discussions must be submitted for individual papers. This paper is part of the ***Journal of Structural Engineering***, © ASCE, ISSN 0733-9445.

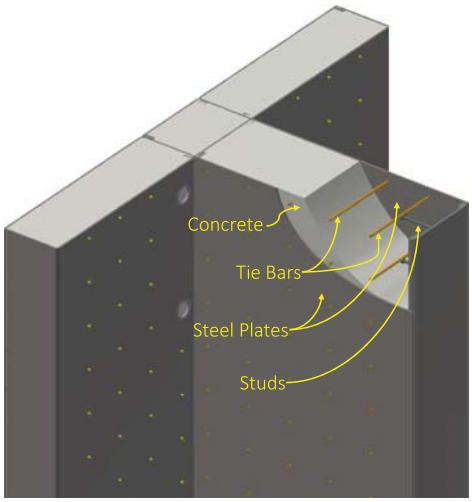

Fig. 1. Main components of T-shaped concrete filled composite plate shear walls (C–PSW/CF).

Alzeni and Bruneau (2014, 2017) tested four cantilever concrete-filled sandwich steel panel (CFSSP) walls with circular boundary elements. The specimens attained and exceeded their plastic moment capacity and showed stable ductility up to 3% drift in both directions. However, again the tests were not performed with axial loadings.

Shafaei et al. (2021) tested five planar C-PSW/CF (having height-to-length ratio of 3) under cyclic horizontal loads and combined constant axial compression (up to 30% of the squash strength of the concrete area, $A_c f'_c$). The overall displacement ductility was greater than 4 from all specimens. In parallel, Kenarangi et al. (2020, 2021) conducted research on C-Shaped walls that had a cross-sectional area at 3/8 scale of the walls in a prototype building (flange length of 9,144 mm (360 in.), web length of 3,048 mm (120 in.), steel plate thickness of 12.7 mm (0.5 in.), flange thickness of 635 mm (25 in.), web thickness of 635 mm (25 in.), tie bar spacing of 304.8 mm (12 in.), and tie bar diameter of 25.4 mm (1 in.), as provided to the research team by a project advisory team), and subjected them to simultaneous axial and cyclic lateral loadings. Given that C-shaped walls can be parts of the lateral-load resisting core of building (around elevator shafts, a number of different cross-section shapes, such as planar walls or C-shaped, T-shaped, L-shaped, and I-shaped walls, can be used individually or as segments of larger core walls), investigating the flexural behavior of such walls was important. However, due to lab constraints, these walls were only tested with a maximum axial load equal to 19% of the crushing load of the infill concrete. Knowledge on the cyclic inelastic flexural behavior of these types of walls when subjected to higher axial loading (up to 30% of the crushing load of the infill concrete), under quasi-static cyclic demands representative of either seismic or wind loading with different cyclic amplitudes and intensities, was desirable for the development of design guidelines when high-rise core-wall steel buildings having C–PSW/CF are used as the primary lateral force resisting system. Furthermore, there was a strong desire by practicing engineers to verify that T-shaped walls would also, on their own, have an adequate cyclic flexural behavior, when simultaneously being subjected to various levels of constant axial loading. Therefore, complementary to the work by Shafaei et al. (2021) and Kenarangi et al. (2020, 2021), four T-shaped C-PSW/CFs (sized to correspond to half of the C-shaped walls previously tested) were tested at the Structural Engineering and Earthquake Simulation Laboratory (SEESL) at the University at Buffalo. The specimens were subjected to axial load ratios of 15% to 30% of $A_c f'_c$. Moreover, walls having different tie bar diameters and spacings along the height of specimens were tested to confirm that cyclic response would not be adversely affected by the relaxation in bar diameter and spacing introduced in the 2022 edition of the AISC Seismic Provisions for Structural Steel Buildings. All four specimens were subjected to a cyclic loading protocol pushing the walls to large inelastic deformations similar to those that would develop during earthquake excitations; one of those was also subjected to a cyclic protocol more representative of wind loading.

Design of Specimens

Test Set-Up Design

Each wall specimen tested was a cantilever embedded at its base into a reinforced concrete footing needed to transfer the base moment into the laboratory strong floor. Therefore, the entire test setup consisted of four main components, namely: (1) the T-shaped C-PSW/CF, (2) the reinforced concrete footing, (3) the lateral loading system (LLS), and (4) the axial loading system (ALS). The corresponding test set-up is illustrated in Figs. 2 and 3.

The height of the wall, from top of the footing to the centerline of the actuator plates was about 4,419.6 mm (14.5 ft.). The total height of the test set-up from the strong floor was 5,029.2 mm (16.5 ft.). Fig. 3(a) shows a schematic 3D view of the T-shaped C-PSW/CF wall.

The intent was to design and test T-shaped walls having a flange width equal to half that of the C–shape wall, similar web dimensions, and same tie bar diameter and spacing [12.7 mm (0.5 in.) in diameter and 152.4 mm (6 in.) spacing]. Moreover, P-M diagrams (based on plastic strength of cross sections) of C- and T-shaped walls were compared, and slight modifications were made to the geometry of the T-shaped walls to ensure similar flexural strengths under identical axial loads. Fig. 3(b) shows the dimensions of the resulting T-shape specimens cross section. Instead of having exactly half of the flange of the C-shaped walls [1,238.25 mm (48.75 in.)], the length of the flange of the T-shaped walls was 1,228.73 mm (48.375 in.) [Fig. 3(b)]. This minor difference occurred because of the additional plates that needed to be placed on the sides of the flange to keep the concrete inside the cross section compared to what would correspond to exactly half of the C-shaped walls cross section. Finite element analyses were also conducted to verify that the inelastic behavior of the entire

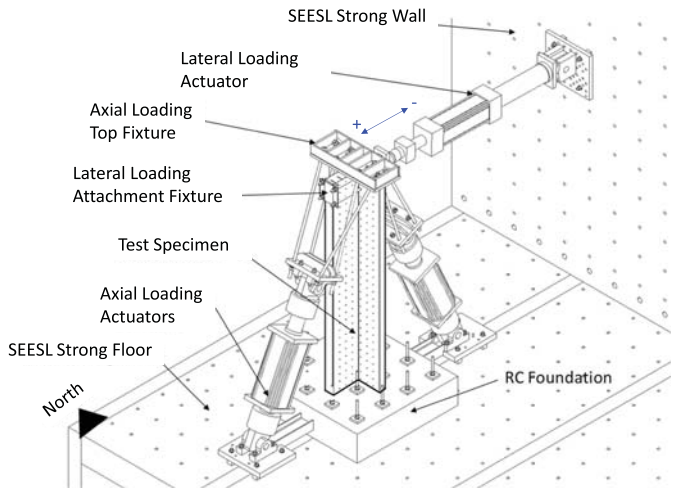

Fig. 2. 3D view of the test setup.

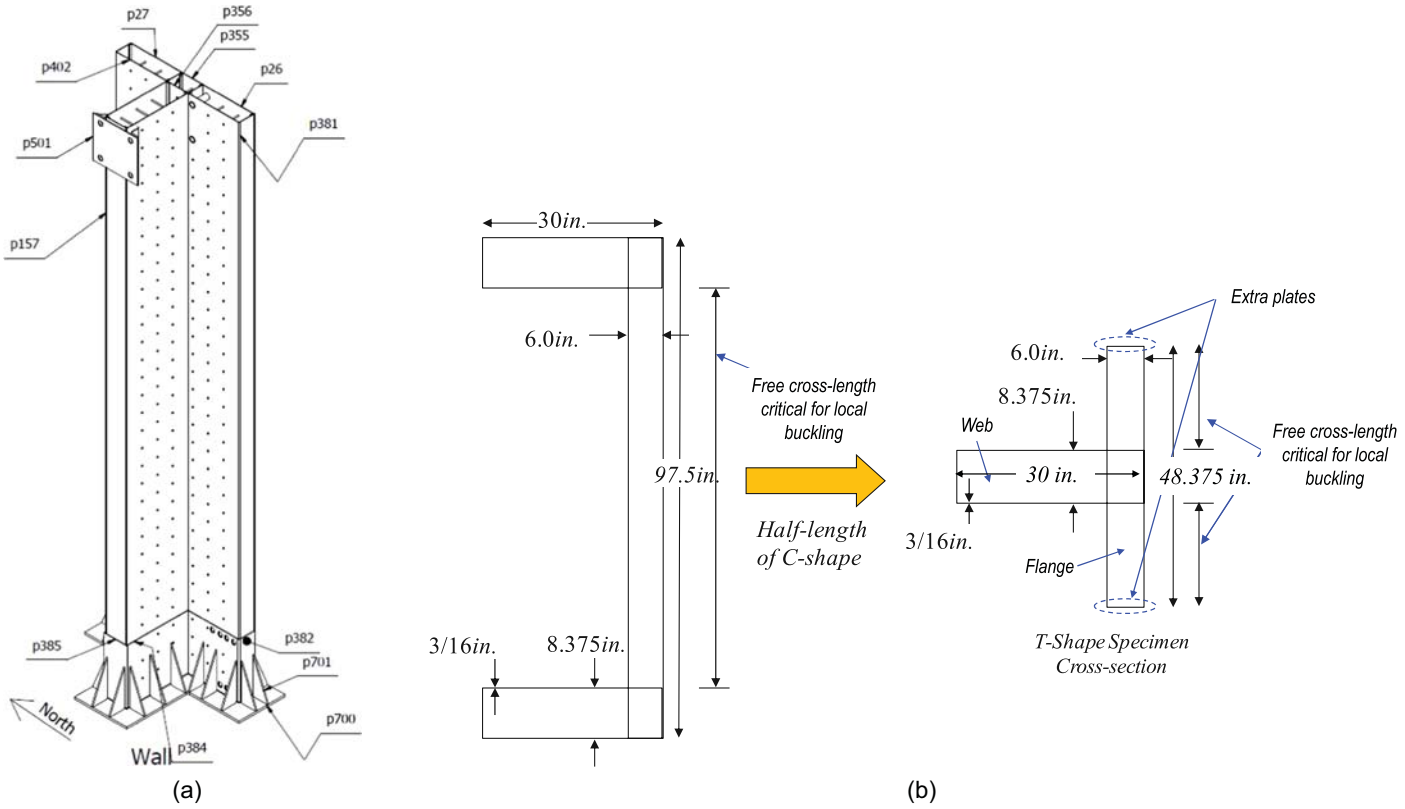

Fig. 3. (a) 3D view of the wall; and (b) T-shape specimen cross-section dimensions.

T-shaped walls specimens bent about their strong axis here would be similar to the inelastic behavior of the C-shaped walls bent about their weak axis.

At the top of the wall, horizontal loading was applied to the specimen's webs, and vertical force was applied to the wall's flange, as illustrated in Figs. 2 and 3. Further details of the test setup can be found in Kizilarslan (2021).

Overview of Testing Program

Initially, only two T-shaped C-PSW/CF were to be tested as part of the test program to be conducted. Upon completion of testing of the C-shaped walls, the project advisory team requested that Specimen T1 be tested instead per a prescribed cyclic wind protocol that imparted cycles up to a yield strain of 1.5 times the yield strain (i.e., 1.5εy). This decision eliminated the ability to compare results of Specimen C2 (Kenarangi et al. 2020, 2021) and Specimen T1 as intended by the original testing program, but provided an opportunity to investigate the specimen cyclic behavior from a wind performance-based design perspective (ASCE 2019). However, the same axial loading as Specimen C2 was applied to Specimen T1 with a hope to test it with a seismic loading protocol if it did not fracture after completion of the wind protocol. To keep the wall elastic within the footing, the details originally developed and submitted to the fabricator had doubler plates added to the wall faces within the footing. These doubler plates consisted of 4.76 mm (3/16 in.) plates fillet weld at the top of existing wall plates; a full penetration (CJP) weld of both plates (i.e., existing wall plate and doubler plate) was proposed where the wall connected to a base plate at the bottom of the footing (Fig. 4). However, for fabrication

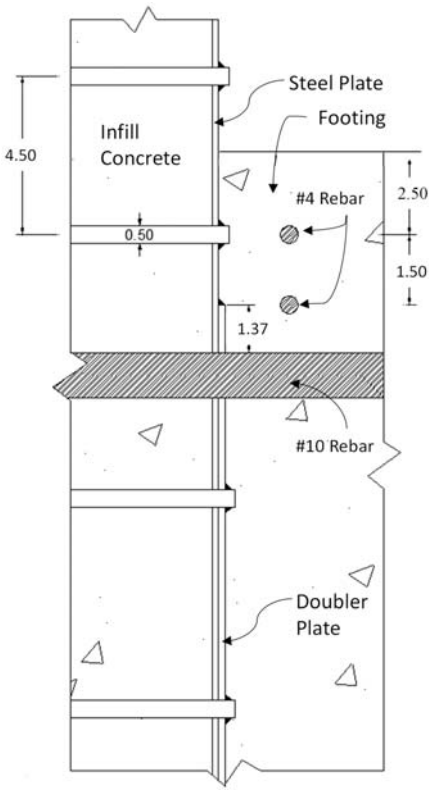

Fig. 4. Doubler plate connection detail near the top of footing (dimensions are in inches).

Table 1. Properties of the T-shape specimens

Wall parameters	Units	T1	T2	T3	T4
Wall height, H	in.	166	166	166	166
Flange length, h	in.	48.375	48.375	48.375	48.375
Web length, b	in.	30.0	30.0	30.0	30.0
Steel plate thickness, t_s	in.	3/16	3/16	3/16	3/16
Flange thickness, d	in.	6.0	6.0	6.0	6.0
Web thickness, c	in.	8.375	8.375	8.375	8.375
Tie spacing (vertical and horizontal)	in.	6	6	4.5	4.5
Tie diameter	in.	1/2	1/2	1/2	1/4
Wall aspect ratio (height to web), H/b	n.a	5.53	5.53	5.53	5.53
Cross-section aspect ratio, $\gamma = b/h$	n.a	0.62 ($=\gamma_p$)	0.62 ($=\gamma_p$)	0.62 ($=\gamma_p$)	0.62 ($=\gamma_p$)
Flange aspect ratio, $\alpha = d/h$	n.a	0.12 ($=\alpha_p$)	0.12 ($=\alpha_p$)	0.12 ($=\alpha_p$)	0.12 ($=\alpha_p$)
Web aspect ratio, $\beta = c/b$	n.a	0.28 ($=t_w$)	0.28 ($=t_w$)	0.28 ($=t_w$)	0.28 ($=t_w$)
Steel area, A_s	in.^{2}	32.9	32.9	32.9	32.9
Concrete area, A_c	in.^{2}	458.4	458.4	458.4	458.4
Gross area, A_g	in.^{2}	491.25	491.25	491.25	491.25
Reinforcement ratio of web, ρ_{web}	%	2.14	2.14	2.14	2.14
Reinforcement ratio of flange, ρ_{flange}	%	4.6	4.6	4.6	4.6
Reinforcement ratio, ρ_s	%	6.7	6.7	6.7	6.7
Yield strength, F_y	ksi	54	54	61.07	60.03
Concrete strength, f'_c	ksi	3.6	5.7	6.03	4.17
Crushing load of concrete, $A_c f'_c$	kips	1,650	2,613	2,662	2,049
Target axial load	kips	247.5	784	799	615

Note: 1 in. = 25.4 mm; 1 ksi = 6.89 MPa; and 1 kip = 4.45 kN.

convenience, the steel fabricator who built the specimens proposed to use instead inside the footing a thicker 9.53 mm (3/8 in.) plate with CJP weld top and bottom to the wall steel plates and base plate, respectively. The specimens were fabricated accordingly. Subsequently, for reasons described later, Specimens T3 and T4 were fabricated with the cover plate details.

Furthermore [as done for the C-shaped C–PSW/CF specimens previously tested by Kenarangi et al. (2020, 2021)], Specimens T1 and T2 were designed per Chapter H7 of AISC-341 (AISC 2016); as a result, the diameter of tie bars and their horizontal and vertical spacing were calculated to be 12.7 mm (0.5 in.) and 152.4 mm (6 in.), respectively. Instead, Specimens T3 and T4 were designed per the upcoming revision of these design provisions [revised Chapter H7 and new Chapter H8 of AISC-341 (AISC 2022) for walls without boundary elements], to have 114.3 mm (4.5 in.) tie spacing. T3 and T4 were also designed with 12.7 mm (0.5 in.) and 6.35 mm (0.25 in.) diameter tie bars, respectively. Also, for Specimens T3 and T4, as shown in Fig. 4, to better protect the fillet weld from possible rotations due to buckling of the wall steel plates (even though that buckling inside the footing was unlikely), an additional row of tie bars was added to the wall, above the fillet weld of the doubler plate, but at 63.5 mm (2.5 in.) from the top of the concrete foundation. Moreover, additional inverted-U shape bars (with horizontal bar length longer than the wall width) were added at various locations along, and close to the face of the wall to prevent spalling of the concrete of the footing over the 101.6 mm (4 in.) distance above the fillet weld. This confined the concrete near the wall inside the footing, to help prevent buckling of the walls steel plates embedded there. Detailed drawings of the specimens can be found in Kizilarslan (2021).

As another improvement for Specimens T3 and T4, studs of same diameter as the tie bars were welded on the web closure plates at 19.1 mm (0.75 in.) to develop buckling at the same level on the closure plate and steel plate between tie bar rows.

Properties of Tested Specimens

Table 1 summarizes many relevant dimensions and properties for the four T-shaped specimens (Fig. 5) tested, namely: overall dimensions; tie spacing and diameter; wall aspect ratios; steel, concrete, and gross areas; reinforcement ratios; yield strength and concrete compressive strength, target axial loads (15% and 30% of crushing load of concrete (i.e., $A_c f'_c$) for Specimen T1; and T2, T3, and T4, respectively).

From test coupons, average yield strength for Specimens T1 to T4 was 372.3 MPa (54 ksi), 372.3 MPa (54 ksi), 420.6 MPa (61 ksi), and 413.7 MPa (60 ksi). Also, for Specimen T3, average yield strength of the 12.7 mm (0.5 in.) diameter tie bars was 613.2 MPa (88.93 ksi). However, for Specimen T4, the 6.4 mm

Fig. 5. Finished test setup of T-shaped wall specimen.

(0.25 in.) diameter tie bars tested fractured prematurely. Only one of them reached post-yield strains and its yield strength was determined to be 643.3 MPa (93.3 ksi). The concrete strength obtained from unconfined concrete cylinder tests done at the start of each wall test for Specimens T1 to T4 were 25.2 MPa (3.65 ksi), 39.3 MPa (5.7 ksi), 41.6 MPa (6.03 ksi), and 28.8 MPa (4.17 ksi), respectively. The reason why different concrete strengths were obtained is unknown even though the same concrete type was ordered from the same supplier and the same curing was done for all concrete cylinders.

Loading Protocol of T-Shape Specimens

These composite walls are intended to be used in buildings located in seismic regions as well as in regions where wind loading is dominant. Seismic and wind loadings have different drift amplitude and intensities (i.e., different number of cycle at different displacement/strain amplitudes). Therefore, the walls were tested to observe the behavior under both loadings to develop an understanding of the behavior for this system in both conditions.

The test protocols were quasi-static cyclic lateral loadings to observe the cyclic inelastic behavior of walls at different drift ratios and intensities. The cyclic inelastic protocol used is consistent with what has been typically done to investigate the cyclic inelastic behavior of members expected to exhibit a stable hysteretic behavior during earthquakes [ATC-24 (ATC 1992); AISC-341 (AISC 2016)]. Except for the large number of inelastic cycles representative of wind loading applied to Specimen T1, where a consensus document does not exist, and the loading protocol was specified as indicated in the following paragraph. These protocols are not intended to provide a displacement history identical to the building's dynamic response during possible seismic or wind loadings, but are deemed adequate to prequalify detailing in compliance with the approach taken by various consensus-based design documents.

Specimen T1 was first tested per a prescribed cyclic wind protocol that imparted cycles up to a yield strain of 1.5 times the yield strain (i.e., $1.5\varepsilon_y$), to provide a limited opportunity to investigate the specimen cyclic behavior from a wind performance-based design perspective (ASCE 2019). Even though there is currently no standard that specifies a cyclic history protocol to be applied to replicate representative wind loading demands up to strains exceeding yield [contrary to the standard cyclic testing protocols that exist in earthquake engineering, which originated with ATC-24 (ATC 1992) and have been since embedded in design specifications such as AISC-341 (AISC 2016)], the members of the project advisory team prescribed the following displacements history: 500 cycle at $\pm 0.5\Delta_y$ (yield displacement), 500 cycles at $\pm 0.75\Delta_y$, 50 cycles at $\pm\Delta_y$, 20 cycles at $\pm 1.5\Delta_y$, 50 cycles at $\pm\Delta_y$, 500 cycles at $\pm 0.75\Delta_y$, and 500 cycle at $\pm 0.5\Delta_y$. It is a protocol that has been used in other projects (Abdullah et al. 2020; Shafaei 2020) and is deemed to be conservative (particularly since, for most structures, wind loading would not produce full load reversal). For the walls tested, the yield displacement, Δ_y, was defined to be the displacement that caused the average steel strain between 1st and 2nd row of tie bars to reach the yield strain. Therefore, in order to predict the yield displacement corresponding to this condition, a finite element analysis (FEA) model of Specimen T1 was run using the expected material behavior of the steel and actual concrete strength. The results showed that the wall yield displacement was 25.4 mm (1 in.), regardless of the direction of loading as the first yield always occurs at the tip of the web plate. In summary, a total of 2,120 cycles of lateral displacements, following the protocol, were applied to the top of Specimen T1 while it was simultaneously subjected to a constant axial load equal to 15% of the concrete crushing load.

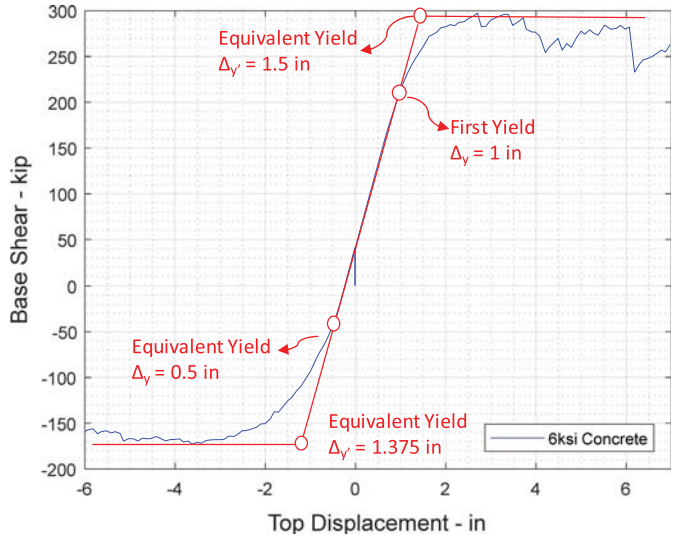

Fig. 6. Pushover result of the FEA model of Specimen T2 and bilinear approximation of the curves in positive and negative directions.

The FEA of the model of Specimen T2 under an axial loading equal to 30% of the concrete crushing load was also performed in order to construct the seismic loading protocol for Specimens T2 to T4. The details of this modeling can be found in Kizilarslan (2021). Due to the higher strength of concrete in that specimen compared to the other specimen, the equivalent yield displacements were measured to be 38.1 mm (1.5 in.) and −34.9 mm (−1.375 in.) in the positive (web in compression) and negative (flange is in compression) directions. Up to the equivalent yield displacements [38.1/ − 34.9 mm (+1.5/ − 1.375 in.)] obtained from the bi-linear envelope of the pushover curves (Fig. 6), Specimen T2 was cycled in a displacement-controlled mode. Two cycles were applied per drift amplitude for the first 10 cycles, after which it was increased to three until the maximum capacity of specimen was reached [114.3/ − 104.9 mm (+4.5/ − 4.13 in.)], and then the number of cycles was decreased to two at each displacement amplitude for the subsequent cycles. Note that the original protocol contained only two cycles at 6% drift, but as will be shown later, the specimen was cycled repeatedly at that drift, as needed to observe the further progression of fracture. Drifts were limited to 6% for safety reasons, to keep the specimen stable after substantial strength degradation.

To compare between specimens, the same loading protocol was used for Specimens T2 to T4.

Test Observations and Results

The centroid of the T-Shaped specimens is located at 225.3 mm (8.87 in.), 226.6 mm (8.92 in.), 225.8 mm (8.89 in.), and 225.0 mm (8.86 in.) from the outside–face of the flange for Specimens T1, T2, T3, and T4 (slight differences are a consequence of the various concrete strength in these specimens). However, for practical reasons, the axial loading could not be applied at the centroid due to practical reasons. This resulted in a moment due to the eccentricity of the axial load, which was taken into account when post-processing the experimental results. During application of the axial loading, the horizontal actuators were locked to prevent the specimens from moving laterally due to the moment created by the axial load

eccentricity. The vertical actuators were driven in a force-controlled mode such as to apply constant axial force to the specimen cross section (this was verified by readings from strain gauges located on the specimen. Then, the specimens were subjected to the cyclic loading protocols.

Test with Wind Loading Protocol

First, the force in each vertical actuator was increased up to 623 kN (140 kips) to apply an axial force equal to 15.3% of $A_c f'_c$ on the cross section of the T-shape wall. Then, the lateral displacements were applied. Throughout the test, the rate of loading was between 80 and 120 *s.* per cycle. Even though FEA was done in order to capture the 0.5, 0.75, 1.0, and $1.5\Delta_y$ displacements for the wind loading protocol, the actual displacements corresponding to these values were decided in real-time on the basis of instrument readings during the test. After the first 500 cycles at $0.5\Delta_y$, and 500 cycles at $0.75\Delta_y$, no fracture or buckling was observed in the specimen. The strain gauge readings showed that at the top displacement of 30.5 mm (1.20 in.), the average of the strain gauges (−1,823, −1,949, and −1,841 $\mu\varepsilon$ in the positive drift direction; and 2,309, 1,901, and 1,998 $\mu\varepsilon$ in the negative drift direction) provided an average strain equal to the average measured yield strain. After 50 cycles, it was observed that the concrete in the footing close to the tip of web closure plate lifted up a bit (but not enough to remove the concrete chunk completely). It was speculated that this might be due to a crack that initiated at the steel plate under the concrete footing. Also, a small buckle was observed on the web.

After the 50 cycles at $1.0\Delta_y$ displacement, the displacement that caused an average strain equal to $1.5\varepsilon_y$ was sought. The wall was cycled twice with 35.6 mm (1.4 in.) displacement. However, the strain gauges between the first and second tie bar rows started to show smaller value than they were showing before, indicating that the values they were reading were not purely axial strains anymore, but rather values distorted due to buckling of the plate. Also, the string potentiometer readings that agreed with the average of the strain gauges in the previous cycles, also started to give illogical readings; this was attributed to the possible rotation of the magnets connecting the instruments to the wall faceplate due to buckling of the steel plate. At this point, the only reliable way remaining to determine the displacement that caused a $1.5\varepsilon_y$ average strain in the critical cross section was to obtain strains from the Krypton data as the LEDs targets used by the Krypton system were still attached to the surface of the wall. In conducting this data analysis, it was decided to look at the strain profiles in the cross section as the data read from LEDs close the tip of the web might have been affected by the steel plate buckling near it. Figs. 7(a–c) show the three strain profiles obtained from LEDs between 1st and 2nd rows of LEDs (located between 1st tie bar and the middle of 1st and 2nd tie bar rows [76.2 mm (3 in.) vertical spacing)], between 2nd and 3rd rows of LEDs (located between the middle of 1st and 2nd tie bar rows and 2nd tie bar row), between 1st and 3rd rows of LEDs (located between 1st tie bar and 2nd tie bar rows) rows at first cycles of each displacement amplitude. The dashed line was later drawn on top based on the average of the three profiles in order to find the strain at the tip of the west face of the web (referred to as WW afterwards). Results from all these average profiles show that the strain on WW was slightly higher than their respective targets at the wall displacements defined as corresponding to 0.5, 0.75, and $1.0\varepsilon_y$. Furthermore, when the wall was further cycled to 36.8 mm (1.45 in.). in both the positive and negative directions to determine the $1.5\Delta_y$ displacement, the strain profile in Fig. 7(d) shows that at that displacement the wall experienced $1.5\varepsilon_y$ at the tip of WW. Therefore, for the remaining 19 cycles at $1.5\varepsilon_y$ it was decided to proceed by cycling at 36.8 mm (1.45 in.) displacement in both directions.

Note that in the non-linear range, the preceding results illustrate the well-known result that curvature ductility grows faster than

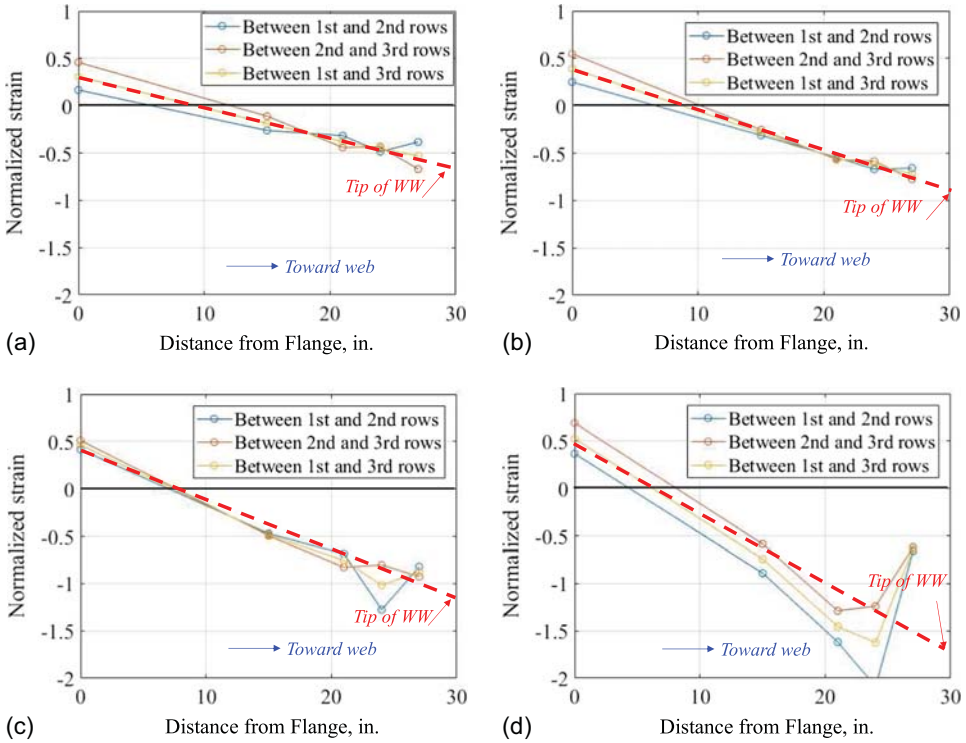

Fig. 7. Strain profiles at peaks of (a) $0.5\varepsilon_y$; (b) $0.75\varepsilon_y$; (c) $1.0\varepsilon_y$; and (d) $1.5\varepsilon_y$ between strains obtained from krypton data at 1st, 2nd, and 3rd rows.

Fig. 8. Onset of buckling steel plate on (a) the north face of the web (NW); (b) the west face of the web (WW); and (c) the south face of the web (SW).

displacement ductility. In order words, if the wall has been cycled to 1.5×30.5 mm (1.2 in.) $(1.0\Delta_y) = 45.72$ mm (1.80 in.) $(1.5\Delta_y)$, the wall would have experience strains greater than the target (and possibly more premature fracture).

During these 20 cycles, progressively, some concrete lifted up at the top of the footing at the tip of WW, then the steel plates between the 1st and 2nd tie bar rows at the north face of the web (referred to as NW afterwards) and at the south face of the web (referred to as SW afterwards), and at 50.8 mm (2 in.) from the top of the footing at WW buckled (Fig. 8); then fracture was detected at the corner of WW and NW at the foundation level (Fig. 9), growing to become 92.1 mm (3.625 in.) long on NW and extending across the entire web on WW. Another fracture was also observed on SW in the late cycles, but its actual length could not be measured as the tip of that crack propagated below the top of the footing.

Then, according to the wind loading protocol, the cycle amplitudes were ramped down to $1.0\Delta_y$ displacement for 50 cycles, $0.75\Delta_y$ displacement for 500 cycles, $0.5\Delta_y$ for 500 cycles, during which cracks propagated further. At end of each cycle amplitude, the measured losses were 49%, 49.5%, and 51.6% of the web cross section, respectively (Fig. 10) (i.e., the average of the fractures on both sides of the web being between 300 and 308 mm (11.8–12.12 in.) out of 609.6 mm (24 in.) of web length). Observations for this test of Specimen T1 are summarized in Table 2.

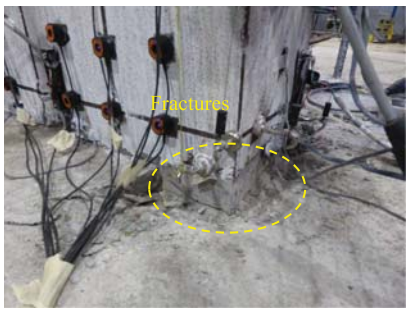

Fig. 9. Fracture in the corner of the north face of the web (NW), and the west face of the web (WW) at 1,060th Cycle.

The specimens were inspected after their failure. Fig. S1 section shows a schematic of the damage on the steel plates for all specimens. In these figures, the locally buckled areas are marked with dashed line, and fractures are shown with a solid line.

After the wind cyclic displacement protocol was completed, Specimen T1 was repaired to allow re-testing, this time by subjecting the specimen to a seismic cyclic displacement protocol (instead of a wind one). An effective repair method was developed and experimentally validated for the previously tested C-shaped specimen (Kizilarslan and Bruneau 2021), but that proven repair procedure was deemed to be too involved for the available resources and too time-consuming at this stage of the project. Therefore, a simpler repair method was attempted, using the tip of a rotary grinder to widen the crack to about 2.39 mm (0.094 in.) [half of the thickness of steel plate, 4.76 mm (0.1875 in.)] and attempt to weld the crack shut along that path. However, this repair weld did not perform efficiently and the weld opened during yield excursions at $2\Delta_y$. More details can be found in Kizilarslan et al. (2021).

Tests with Seismic Protocols

In Specimen T1, it was observed after removing some concrete from the top of the footing that cracking had initiated just above the CJP weld connecting the wall steel plate to the thicker plate embedded in the concrete footing, and did so at the edge of the web closure plate (i.e., in the corner of the web where the wall plates orthogonal to each other were joined by a vertical weld). Therefore, before casting any concrete for Specimen T2, the horizontal CJP welds connecting the 4.76 mm (3/16 in.) thick plates of the wall to the 9.53 mm (3/8 in.) embedded plates of Specimen T2 were inspected by certified weld inspectors who performed visual inspection, magnetic particle inspection, ultrasonic inspection, and radiographic inspection. Visual inspection revealed that the welds in the corners were a cause of concern, as the welder apparently stopped/started all welds at these corners, which left the corners not fully welded. Magnetic inspections did not reveal any surface openings in the weld. Ultrasonic inspection detected porosity in welds at critical locations (most importantly at the corners that were already identified as problematic by visual inspection, and at some locations along the flange). X-ray photos from radiographic

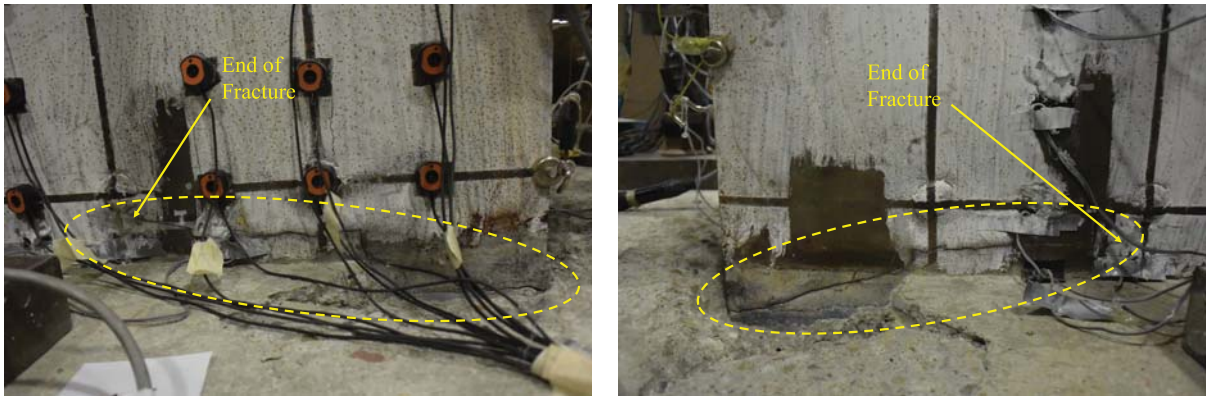

Fig. 10. Fractures after test is complete and local removal of concrete at (a) north face of the web (NW); and (b) south face of the web (SW).

Table 2. Experiment log of Specimen T1

Cycle No.	Cycle drift, in.	Laterally applied force, V, kips	NW	WW	SW	FE	FW
500	0.58/ − 0.65	44.35/ − 33.8	—	—	—	—	—
1,000	0.9/ − 0.9	51.9/ − 34.8	—	—	—	—	—
1,050	1.2/ − 1.2	82.6/ − 63.0	Slight B@1st–2nd TR	—	Slight B@1st–2nd TR	—	—
1,060	1.45	**92.7**	B @1st–2nd TR	B @2in. FF	B @1st–2nd TR	—	—
	−1.45	**−63.2**	3.19in. FR	5.25in. FR	—	—	—
1,065	1.45/ − 1.45	88.6/ − 51.2	3.63in. FR	8.38in. FR	Cannot be measured	—	—
1,120	1.2/ − 1.2	63.2/ − 34.2	4.75in. FR	—	Cannot be measured	—	—
1,220	0.9/ − 0.9	36.3/ − 17.7	8.25in. FR	—	Cannot be measured	—	—
1,320	0.9/ − 0.9	38.1/ − 14.1		35.4% FR		—	—
1,420	0.9/ − 0.9	36.4/ − 13.3		38.5% FR		—	—
1,520	0.9/ − 0.9	35.5/ − 11.7		45.3% FR		—	—
1,620	0.9/ − 0.9	35.0/ − 11.1		47.4% FR		—	—
1,720	0.58/ − 0.65	15.6/ − 9.6		48.7% FR		—	—
1,820	0.58/ − 0.65	15.2/ − 9.6		49.0% FR		—	—
1,920	0.58/ − 0.65	14.6/ − 10.1		49.5% FR		—	—
2,020	0.58/ − 0.65	14.1/ − 10.05		50.5% FR		—	—
2,120	0.58/ − 0.65	14.0/ − 9.9		51.6% FR		—	—

Note: Bold values are for the maximums in positive and negative excursions. The steel plate faces are abbreviated as follows: NW = the north of web; WW = the west of web; SW = the south of web; FE = the east of flange; and FW = the west of flange. Also, FF means *from footing*, FR is fracture, B is buckling, and TR is tie bar row. 1 in. = 25.4 mm; 1 ft = 0.3048 m; and 1 kip = 4.45 kN.

inspection confirmed the presence of porosities in the welds at the corners and in the flange welds. However, in spite of these significant defects, it was decided to proceed with testing of Specimen T2, because it was available and could still provide meaningful results [Styrofoam blocks were located at these corners before pouring the concrete footing, and removed afterwards to allow observing the welds during the test as shown in Figs. 11(a and b)]. However, Specimens T3 and T4 were then fabricated (as indicated earlier) to provide better details avoiding all these observed problems.

Note that since Specimens T2, T3 and T4 were subjected to the same loading protocols, but fabricated differently as indicated earlier, results for these three specimens are presented together here. The forces in each vertical actuators were increased up to 1,890.5 kN (425 kips) (maximum force) to apply an axial load equal to 30% of the concrete crushing load ($A_c f'_c$) to the cross section of the T-shape wall. Then, the lateral actuators applied the lateral displacements at the top of the specimen according to the predetermined cyclic loading protocol.

None of the steel plates of the specimen experienced any buckling or yielding through all of the excursions cycles at amplitudes of $\Delta_y/4$, $\Delta_y/2$, and $3\Delta_y/4$. At the positive peak of the estimated displacement of Δ_y, no local buckling was observed.

At the lateral displacement equal to $2\Delta'_y$ [76.2/ − 69.85 mm (3/ − 2.75 in.)] (i.e., Cycle 17), a maximum lateral force of −443.5 kN (−99.7 kips) was reached in the negative drift direction for Specimen T2. In the third excursion of the same drift (i.e., Cycle 19), a maximum force of 734 kN (165 kips) was reached in the positive direction. For Specimens T3 and T4, maximum positive and negative lateral forces were reached at the displacement amplitude of $1.5\Delta'_y$ [57.2/ − 52.3 mm (2.25/ − 2.06 in.)] (i.e., Cycle 14), and in the first cycle of $3\Delta'_y$ displacement [114.3/ − 104.9 mm (4.5/ − 4.13 in.)] (i.e., Cycle 20) [775.8/− 515.6 kN (174.4/ − 115.9 kips) for Specimen T3 and 645.9/ − 495.5 kN (145.2/ − 111.4 kips) for Specimen T4], respectively.

Buckling

The strain gauge profiles were linear until the estimated yield displacement of Δ_y. At the positive peak of the estimated yield displacement of Δ_y, the strains recorded at the farthest end of the web

Fig. 11. Exposed welds: (a) before concrete pour of footing; and (b) during test.

and flange were −2,532 μstrain and 679 μstrain, which correspond to 136% and 36.5% of the average measured yield strain (i.e., 1,862 μstrain) of the steel plate based on the coupon tests, for Specimen T2. The strains recorded at the same displacement were −82.1% and 20.7% of the average measured yield strain (i.e., 2,106 μstrain based on coupons for Specimen T3) for Specimen T3 and −92.4% and 34.2% of the average measured yield strain (i.e., 2,070 μstrain based on coupons for Specimen T4) for Specimen T4. In the second excursion at the same drift, the strain values did not change much. No local buckling was observed in all specimens at this cycle amplitude.

At the displacement amplitude of $1.5\Delta_y'$ [57.2/ − 52.3 mm (2.25/ − 2.06 in.)] (i.e., Cycle 14), local buckling initiation was observed between the 1st and 2nd tie row bars on NW and SW in all specimens. Moreover, at the same cycle, the steel plate on WW also buckled at 50.8 mm (2 in.) from the top of the footing in Specimen T2 and at 88.9 mm (3.5 in.) in Specimens T3 and T4. This showed that welding studs on the closure plate helped to move buckling up to the same level as buckling between 1st and 2nd tie bar rows on the sides as intended. In the negative direction of the lateral displacement equal to $2\Delta_y'$ [76.2/ − 69.85 mm (3/ − 2.75 in.)] (i.e., Cycle 17), buckling started to initiate on the east side of flange (referred to as FE afterwards) of Specimen T2, specifically between the 1st and 2nd tie rows on the north side of FE and between 2nd and 3rd tie rows on the south side of FE. The same buckling happened in the negative excursion of the first cycle of $3\Delta_y'$ displacement [114.3/ − 104.9 mm (4.5/ − 4.13 in.)] (i.e., Cycle 20) in Specimen T3 and in the negative drift of the third excursion at the $2\Delta_y'$ displacement [76.2/ − 69.85 mm (3/ − 2.75 in.)] (i.e., Cycle 19). The steel plate on the south side of FE buckled between the 1st and 2nd tie bar rows in Specimen T4 but north side of FE did not buckle until $4\Delta_y'$ {i.e., negative peak of Cycle 23 [152.4/ − 139.7 mm (6/ − 5.5 in.)]}. As the wall displaced more, more buckling was observed. Details are found in Tables 3–5.

Fracture

For Specimen T2, in the negative excursion at the lateral displacement equal to $2\Delta_y'$ [76.2/ − 69.85 mm (3/ − 2.75 in.)] (i.e., Cycle 17), a fracture was observed in the corner of WW and SW, 50.8 mm (2 in.) long on the WW side and 38.1 mm (1.5 in.) on the SW side. In Cycle 19, the fracture extended through the entire width of WW and the fracture length on SW was 50.8 mm (2 in.). A new 25.4 mm (1 in.) fracture was observed on NW. In the first excursion of $3\Delta_y'$ displacement [114.3/ − 104.9 mm (4.5/ − 4.13 in.)] (i.e., Cycle 20), where the lateral horizontal force dropped by about 8.9% in the positive displacement direction and by 19.5% in the negative drift, the fractures were 76.2 mm (3 in.) on NW and 114.3 mm (4.5 in.) on SW, i.e., 15.6% of the web was lost [the average of the fractures on both sides of the web being 95.25 mm (3.75 in.) out of 609.6 mm (24 in.) of web length]. Cracks continued to grow in subsequent cycles and failure of welds around some tie bars was also observed [refer to Kizilarslan et al. (2021) for more details]. At the end of test, 81.3% of the web cross section was lost.

For Specimen T3, first, two 76.2 mm (3 in.) long vertical cracks were observed in the corners of WW and NW, and WW and SW between the levels of 1st and 2nd tie bar rows in Cycle 22. Horizontal fracture was not observed until at the positive drift of Cycle 22 [114.3/ − 104.9 mm (4.5 in./ − 4.13 in.)]. Then, during the negative drift of this cycle, a loud noise was heard, and it was observed that an 203.2 mm (8 in.) long fracture had developed on both SW and NW and fractured all through on WW, i.e., 33.33% of the web was lost (the average of the fractures on both sides of the web being 203.2 mm (8 in.) out of 609.6 mm (24 in.) of web length). However, the fracture on NW was 76.2 mm (3 in.) inside from WW. In other words, vertical fracture in the corner did not meet with the fracture in the web between tie bar rows. This implies that, contrary to Specimens T1 and T2, the horizontal fracture started at the apex of the buckled shapes in plates between rows of ties above the footing. In other words, fractures here did not start at the weld between the wall plate and the doubler steel plate cross section embedded into the footing for Specimens T3 and T4. This indicates that the horizontal fracture was genuinely attributable to stress demands and low cycle fatigue of the buckled steel plate (as one would expect under repeated inelastic buckling); it was also unrelated to the vertical fractures that initiated in the earlier cycle. At the end of the test, 87.5% of the web cross section was lost.

For Specimen T4, the behavior was similar to Specimen T3. The first vertical steel fracture was observed in the corner of WW and SW between the 1st and 2nd tie bar rows in Cycle 21 [114.3/ − 104.9 mm (4.5/ − 4.13 in.)]. In the last excursion at the same drift (i.e., Cycle 22), another vertical fracture occurred in the corner of WW and NW between the levels of 1st and 2nd tie bar rows. In the negative direction, horizontal fractures initiated at the corners; 19.05 mm (0.75 in.) on SW and 38.1 mm (1.5 in.) on NW between 1st and 2nd tie bar rows. In the negative direction of the displacement at a drift equal to $4\Delta_y'$ [152.4/ − 139.7 mm

Table 3. Experiment log of Specimen T2

Cycle No.	Cycle drift, in.	Laterally applied force, V, kips	NW	WW	SW	FE	FW
14	2.25/ − 2.06	145.8/ − 93.8	B @1st–2nd TR	B @2in. FF	B @1st–2nd TR	—	—
15	2.25/ − 2.06	136.9/ − 91.9	—	—	—	—	—
16	2.25/ − 2.06	133.8/ − 90.6	B @5th–6th TR	—	—	—	—
17	3.0/ − 2.75	149.6/ − **99.7**	—	B @12in. FF 2in. FR	1.5in. FR	B @1st–2nd TR (North) B @4th–5th TR (North) B @2nd–3rd TR (South)	—
18	3.0	**165.0**	—	—	—	—	—
	−2.75	−91.5	—	3in. FR	—	—	—
19	3.0	156.9	—	—	—	—	—
	−2.75	−86.3	1in. FR	FR through	2in. FR	—	—
20	4.5	150.3	—	B @16in. FF	B @3rd–4th TR	—	—
	−4.125	−80.2		15.6% FR		—	—
21	4.5	118.9	—	—	—	—	—
	−4.125	−71.5		20.1% FR		—	—
22	4.5	111.9	—	—	—	—	—
	−4.125	−64.2		27.6% FR		—	—
23	6	113.8	B @2nd–3rd TR B @4th–5th TR	—	B @2nd–3rd TR	—	—
	−5.5	−67.9		30.7% FR		—	—
24	6	96.2	—	—	—	—	—
	−5.5	−60.7		31.3% FR		—	—
25	7.5	92.8	WFR @1r2c, 2r2c	—	—	2in. FR (middle)	B @1st–2nd TR (South)
	−6.88	−60.5		51.8% FR		B @1st–2nd TR (middle) B @2nd–3rd TR (middle)	—
26	7.5	80.5	—	—	—	—	B @1st–2nd TR (North)
	−6.88	−46.5		56% FR		—	—
27	9	78.4	WFR @2r3c	—	—	1.19in. FR (North)	—
	−8.25	−42.6		74% FR		B @1st–2nd TR (South)	—
28	9	65.3	—	—	—	11in. FR (middle) 1.5in. FR (North)	—
	−8.25	−36.8		78.6% FR		B @FF-1st TR (middle)	—
29	9	56.2	—	—	—	12in. FR (middle) 2in. FR (North)	—
	−8.25	−33.5		79.1% FR		—	—
30	9	49.2	—	—	—	2.25in. FR (North)	—
	−8.25	31.8		81.3% FR		—	—

Note: Bold values are for the maximums in positive and negative excursions. The steel plate faces are abbreviated as follows: NW = the north of web; WW = the west of web; SW = the south of web; FE = the east of flange; and FW = the west of flange. Also, FF means *from footing*, FR is fracture, B is buckling, TR is tie bar row, WFR is tie bar weld fracture, r is tie bar row, and c is tie bar column. 1 in. = 25.4 mm; 1 ft = 0.3048 m; and 1 kip = 4.45 kN.

(6/ − 5.5 in.)] (i.e., positive peak of Cycle 23), where the drop in lateral horizontal force in the positive direction was 54.7%, and 39.6% in the negative direction, the fractures were 254 mm (10 in.) on NW and 273.1 mm (10.75 in.) on SW, i.e., 43.2% of the web was lost [the average of the fractures on both sides of the web being 263.5 mm (10.375 in.) out of 609.6 mm (24 in.) of web length]. At the end of the test, 73.4% of the web cross section was fractured. Note that for this specimen, lots of the welds around tie bars fractured. The punching manner in which they fractured out of the weld suggests that this might have been avoidable if the fillet welds to the ties had not been ground by the fabricator against the original design intent [as reported in Kizilarslan et al. (2021)].

Figs. 12 and 13 show the progressive development of the phenomena described previously at the north-west, south-west corners of the web, and east of flange for Specimens T2, and T3. Also, the details on the progression of buckling and fracture are tabulated in Tables 3–5 for Specimens T2, T3 and T4, respectively.

The specimens were inspected after their failure. The pictures of the specimen in all directions are also shown in Fig. 14. Fig. S2 shows a schematic of the damage on the steel plates for all specimens. In these figures, the locally buckled areas are marked with dashed line, fractures are shown with solid line, the failed welds around tie bars are shown with solid blue lines. Note that these weld failures around tie bars, in all observed cases, were due to weld failure at their connection at only one end of each tie bar, and not because of fracture of the tie bars.

Test Data Analysis

The experimental results of the applied lateral force versus top lateral drift curves for Specimens T1, T2, T3 and T4 are shown in Figs. 15(a–d) [note that Fig. 15(a) is the result from the wind cyclic test protocol, but Figs. 15(b–d) are from the seismic cyclic test protocol], respectively. The vertical axis is the horizontal force applied to each specimen, which is equal to the value recorded by the lateral actuators (note that this is *not* the shear force applied to the specimen, as the horizontal components of the vertical actuator forces was not yet corrected by subtracting the force recorded by the

Table 4. Experiment log of Specimen T3

Cycle No.	Cycle drift, in.	Laterally applied force, V, kips	NW	WW	SW	FE	FW
14	2.25/ − 2.06	**174.4**/ − 95.3	B @1st–2nd TR	B @3.5in FF	B @1st–2nd TR	—	—
15	2.25/ − 2.06	163.1/ − 94.6	—	—	—	—	—
16	2.25/ − 2.06	150.4/ − 93.9	—	—	—	—	—
17	3.0/ − 2.75	168.7/ − 106.6	—	—	—	—	—
18	3.0	157.6	—	—	—	—	—
	−2.75	−104.2	—	—	—	—	—
19	3.0	148.7	—	—	—	—	—
	−2.75	−120.8	—	—	—	—	—
20	4.5	154.9	B @2nd–3rd TR	—	B @2nd–3rd TR	B @1st–2nd TR (North) and B @2nd–3rd TR (South)	—
	−4.125	**−115.9**	—	—	—	—	—
21	4.5	131.4	—	—	—	—	—
	−4.125	−110.0	—	—	—	—	—
22	4.5	116.5	3in. vertical FR	—	3in. vertical FR	—	—
	−4.125	−83.4		33.3% FR		—	—
23	6	109.4	—	—	WFR @3r1c, 3r2c	—	—
	−5.5	−54.2		64.1% FR		—	—
24	6	91.9	B @3rd–4th TR	—	B @3rd–4th TR	—	—
	−5.5	−46.4		65.6% FR		—	—
25	7.5	88.1	WFR @3r2c	—	WFR @3r3c, 2r1c	—	B @1st–2nd TR (South)
	−6.88	−44.3		75.8% FR		B @1st–2nd TR (Middle) and B @2nd–3rd TR (Middle)	—
26	7.5	76.1	—	—	—	—	B @1st–2nd TR (North)
	−6.88	−40.0		77.6% FR		—	—
27	9	77.6	—	—	WFR @2r2c	—	—
	−8.25	−38.1		83.3% FR		—	—
28	9	66.3		87.5% FR		—	—
	−8.25	−35.4				—	—
29	9	59.3				—	—
	−8.25	−33.9				—	—
30	9	54.9				—	—
	−8.25	−32.7				—	—

Note: Bold values are for the maximums in positive and negative excursions. The steel plate faces are abbreviated as follows: NW = the north of web; WW = the west of web; SW = the south of web; FE = the east of flange; and FW = the west of flange. Also, FF means *from footing*, FR is fracture, B is buckling, TR is tie bar row, WFR is tie bar weld fracture, r is tie bar row, and c is tie bar column. 1 in. = 25.4 mm; 1 ft = 0.3048 m; and 1 kip = 4.45 kN.

horizontal actuator). The lateral drift was calculated by dividing the lateral displacement at the top by the distance from the top of the foundation to the centerline of the lateral actuator's attachment head, which is 4,216.4 mm (166 in.) for all specimens. The key observations during the test such as the onset of visible local buckling on the web and flange, and maximum strengths at negative and positive displacements are marked on these curves.

The moment at the base of the walls was calculated by considering the contributions of the horizontal components of the force of the two vertical inclined actuators for axial loading and the horizontal force from horizontal actuator for lateral loading. The east and west actuators used for the axial load application were placed with an inclination angle measured during each test and used in data analysis). These angles are from the strong floor to the actuator, as shown in Fig. 16. The trajectories of the axes of these actuators intersect above the centerline of the flange of the wall. As walls are cycled, the inclination angles of the vertically inclined actuators change. The horizontal actuators carry an extra force developed by their horizontal force component. The free-body diagram of the forces (at zero displacement) is shown in Fig. 16. The moment resisted by the wall at its base was calculated according to the free-body diagram shown in Fig. 16 by Eq. (1) [note that the moment determined by Eq. (1) could not be verified by load cells during tests as it was not possible to install load-cells under the footing, but results from FEA of the specimens showed close agreement between FEA results and moments obtained from Eq. (1) (Kizilarslan 2021)]:

$$\overrightarrow{\boldsymbol{M}_{\mathbf{base}}} = \overrightarrow{\boldsymbol{r}_{\mathbf{act}}} \times \overrightarrow{\boldsymbol{F}_{\boldsymbol{H}}} + \overrightarrow{\boldsymbol{r}_{\mathbf{top}}} \times (\overrightarrow{\boldsymbol{F}_{v1}} + \overrightarrow{\boldsymbol{F}_{v2}}) \tag{1}$$

To determine the ductility (μ), an effective yield displacement ($\delta_{y,eff}$) was considered as the displacement at the intersection of a line tangent to the initial slope of the hysteretic curve and a horizontal line set at the level of the maximum base moment obtained from testing, $M_{base,max}$. The displacement obtained at $0.8M_{base,max}$ after post-peak of the backbone curve of the test setup was taken for the ultimate displacement (δ_u). Then, using Eq. (2), ductility was calculated as 2.13/ − 3.23, 3.07/ − 2.77, and 2.29/ − 2.60 for Specimens T2, T3, and T4, respectively. The ductility of Specimen T1 is not provided here as it was a mostly elastic wind loading protocol that was applied to this specimen

Table 5. Experiment log of Specimen T4

Cycle No.	Cycle drift, in.	Laterally applied force, V, kips	NW	WW	SW	FE	FW
14	2.25/ − 2.06	**145.2**/ − 89.1	—	—	B @1st–2nd TR	—	—
15	2.25/ − 2.06	138.4/ − 88.6	—	B @3.5in FF	—	—	—
16	2.25/ − 2.06	132.5/ − 87.8	—	—	—	—	—
17	3.0/ − 2.75	143.2/ − 101.1	B @1st−2nd TR	—	—	—	—
18	3.0	132.5	—	—	—	—	—
	−2.75	−98.6	—	—	—	—	—
19	3.0	125.3	—	—	—	—	—
	−2.75	−96.5	—	—	—	B @1st–2nd TR (South)	—
20	4.5	123.7	—	—	WFR @2r2c	—	—
	−4.125	**−111.4**	—	—	—	—	—
21	4.5	95.4	WFR @2r2c, 2r3c, 1r4c	—	WFR @3r1c	—	—
	−4.125	−105.2	—	—	—	B @1st–2nd TR (Middle)	—
22	4.5	76.2	WFR @1r1c	—	WFR @2r1c, 2r3c	—	—
	−4.125	−95.4	0.75in. FR	—	1.5in. FR	—	—
23	6	65.7		43.2% FR		—	—
	−5.5	−67.3				B @1st–2nd TR (North)	—
24	6	47.8	—	—	WFR @2r4c, 4r1c, 4r2c	—	—
	−5.5	−48.8		48.4% FR		—	—
25	7.5	47.5		60.0% FR			B @1st–2nd TR (North)
	−6.88	−46.3				—	—
26	7.5	38.6		63.0% FR		—	—
	−6.88	−40.4				—	—
27	9	40.6		71.4% FR		—	—
	−8.25	−38.7				—	—
28	9	31.3		73.4% FR		—	—
	−8.25	−34.6				—	—
29	9			**Skipped**			
	−8.25						
30	9			**Skipped**			
	−8.25						

Note: Bold values are for the maximums in positive and negative excursions. The steel plate faces are abbreviated as follows: NW = the north of web; WW = the west of web; SW = the south of web; FE = the east of flange; and FW = the west of flange. Also, FF means *from footing*, FR is fracture, B is buckling, TR is tie bar row, WFR is tie bar weld fracture, r is tie bar row, and c is tie bar column. 1 in. = 25.4 mm; 1 ft = 0.3048 m; and 1 kip = 4.45 kN.

$$\mu = \frac{\delta_u}{\delta_{y,eff}} \tag{2}$$

In Table 6, the ratio of plastic moment to first yield moment also provides information as to how much of the wall yielded along its height. Results indicate that over roughly 35%–49% of the height of the wall experienced yielding during the test based on actual material properties (i.e., from coupons and cylinder tests).

The plots in Figs. 17(a–d) show the points of maximum flexural strength experimentally obtained for all specimens compared to their corresponding values predicted by theoretical P-M interaction curves (again, using actual material properties). The vertical axis was normalized by the concrete crushing load, $A_c f'_c$, and the horizontal axis was normalized by the corresponding plastic moments based on the direction of bending (+ if the web of cross section is under compression and - if the flange is under compression) with no axial loading. The maximum applied moment from experiments exceeds their value from the corresponding P-M interaction curves.

The calculated moment at the base of the walls were also compared to their theoretical plastic moment calculated using the plastic stress distribution method (PSDM), M_{PSDM}, and to the yield moment, M_y. Note that values of the yield moment and corresponding neutral axis location were calculated for strain diagrams obtained assuming an E_c value obtained using equation in Section 19.2.2 of ACI 318-14. Three different theoretical values were calculated using the actual, nominal, and expected material properties. These comparisons are shown in Figs. 18(a–d) for all specimens [note that Fig. 18(a) is the result from the wind cyclic test protocol, but Figs. 18(b–d) are from the seismic cyclic test protocol]. The actual values are those obtained from the testing of steel coupons of samples from the wall's web and flanges, and of concrete cylinder cast during construction of the walls and tested on the corresponding specimen test day. The nominal yield value used for the steel plates was equal to 345 MPa (50 ksi) (A572Gr50 steel used in the wall's construction). The nominal value for concrete was taken equal to 41 MPa (6 ksi) for all specimens. The expected values for the steel yield and concrete compressive strengths were obtained by multiplying the nominal values by $R_y = 1.1$ and $R_c = 1.5 \times 0.85$, respectively. One would typically expect these values to be close, but this is not a guarantee by itself. However, the difference is indeed large here. The main reason for this difference is because of the low actual concrete strength obtained from the cylinder concrete compression tests. Most particularly, the concrete strengths obtained for Specimens T1 and T4 were 25 MPa (3.65 ksi) and 28.8 MPa (4.17 ksi), respectively, for concrete that was ordered to be 41.3 MPa (6 ksi)—making the specified strength itself 64% and 44% larger than the actual one—and the opposite of what one would expect, as actual strength should typically be larger than

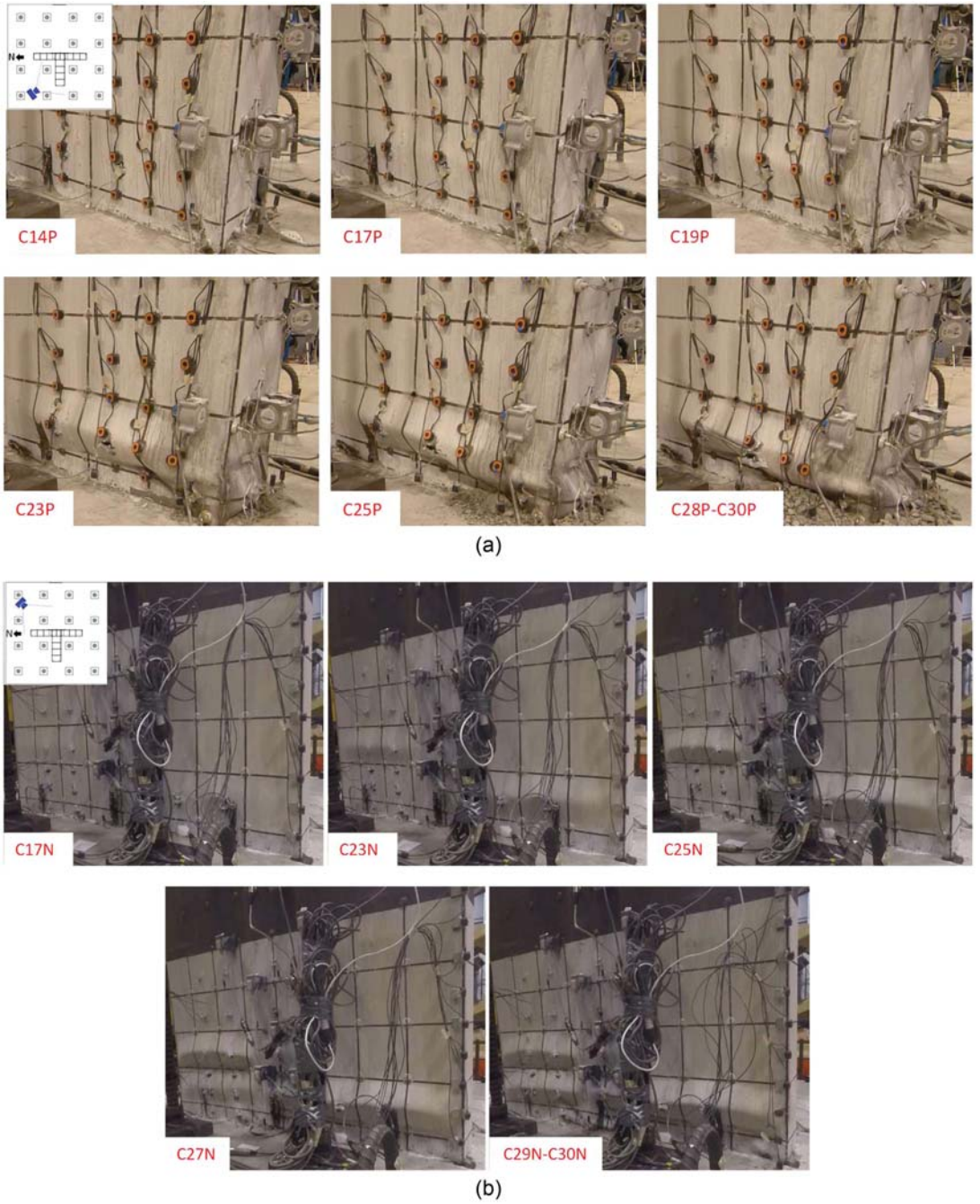

Fig. 12. Development of local buckling at lower part of Specimen T2 at different peak displacements at (a) the north web (NW); and (b) the east face of flange (FE).

specified strength. It is unknown why such a low strength was obtained. Furthermore, the expected value specified by AISC is by definition quite high: for a 41.3 MPa (6 ksi) specified concrete strength, the expected concrete strength is $1.5 \times 0.85 \times 41.3$ MPa $= 53$ MPa (7.65 ksi). By itself, that is 27% more that the nominal concrete strength. Compounding these two effects, the difference between actual and expected plastic moments end-up being 42% and 33% for Specimens T1 and T4 (note: these are lower percentages than obtained multiplying the preceding percentages because only about a third of the cross-section flexural strength comes from concrete; for example, for Specimen T4, 38.5% of M_p comes from concrete in the actual plastic moment calculation, and the number is 31% for the expected plastic moment calculation, the rest of the flexural strength being provided by the steel. All of this information, the material property values, as well as the calculated theoretical strengths are presented in Table 6.

The rotations of the walls at the base where the plastic hinge occurred were also calculated. Vertical string potentiometers were intended to be used. However, the magnets connecting their ends rotated toward the end the tests, and full data was not obtained from these instruments. Instead, the recorded horizontal movements of the string pot attached to the wall and closest to the foundation were utilized. Its readings were divided by its distance to the top of the foundation [838.2 mm (33 in.)]. This resulted in *total* rotations at the wall base (i.e., θ_{wt}), which included the rotations of the wall-foundation connection (i.e., θ_{wf}). The rotations at the

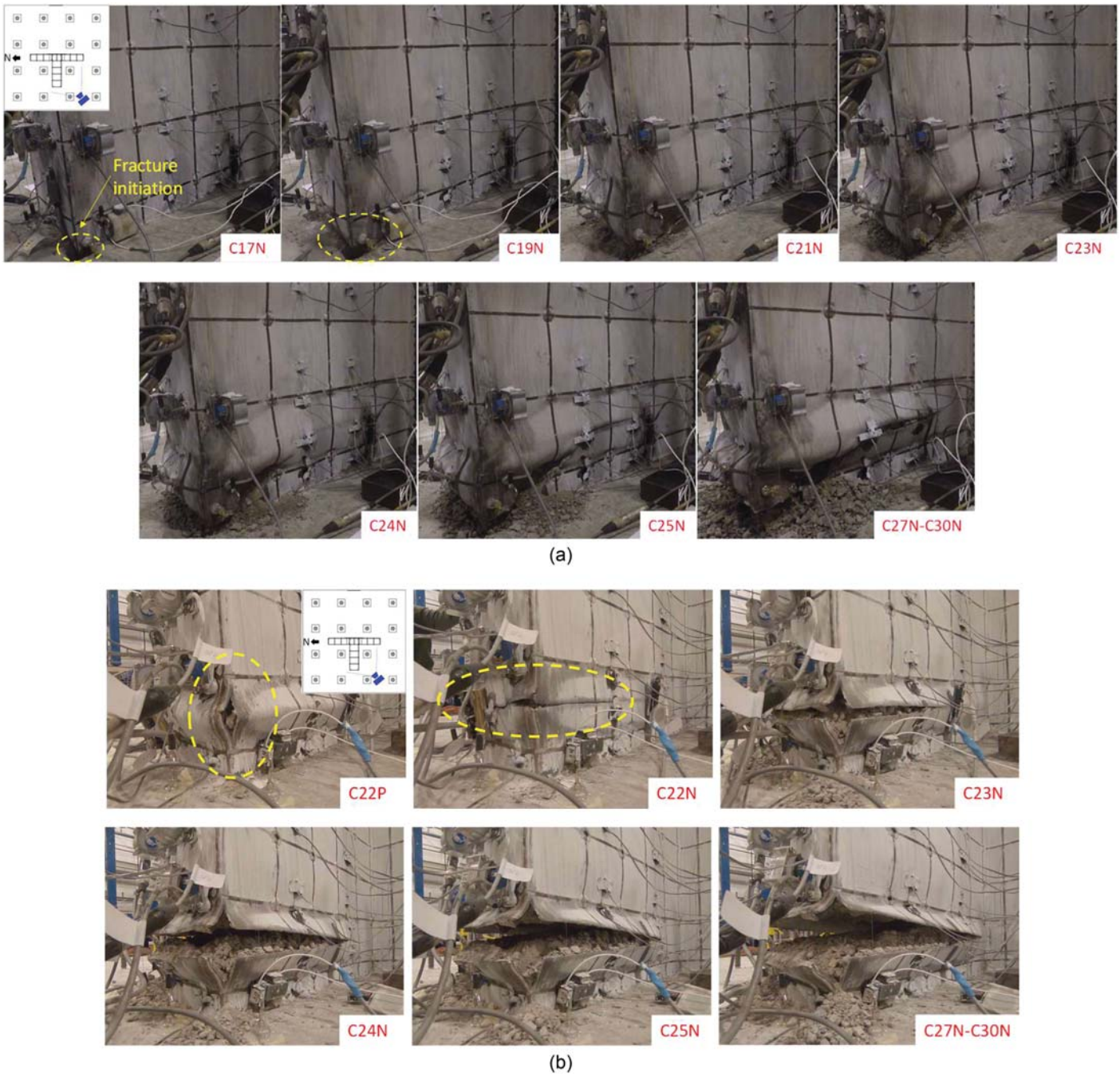

Fig. 13. Development of fracture at lower parts of Specimens (a) T2; and (b) T3 at different peak displacements at the south web (SW).

wall-foundation connection (θ_{wf}) were subtracted from the total rotations (θ_{wt}) to obtain the wall rotations at the base (i.e., θ_{wb}). The wall rotations at the base (i.e., θ_{wb}) at maximum strengths are $0.012/-0.007$, $0.00724/-0.0113$, and $0.006/-0.0107$ for Specimens T2, T3 and T4, respectively. The maximum rotations when flexural strength dropped to 80% of the peak value developed are calculated as $0.021/-0.022$, $0.022/-0.016$, $0.015/-0.015$ for Specimens T2, T3 and T4, respectively. The maximum positive rotation of Specimens T2 and T3 are almost the same but Specimen T4 had the smallest base rotation among all specimens. On the contrary, the maximum rotation of Specimen T2 in the negative direction is higher than that for the others. Specimens T3 and T4 have almost the same maximum base rotation in the negative direction.

Note the wall-foundation connection rotation was taken into account by substituting the foundation and wall-to-foundation connection with a linear rotational spring at the base of the wall. The rotational stiffness of this spring was calculated by finding the slope of a line that was fitted to the M_{base}-θ_{wf} relationship curve in the linear cycles (i.e., the slope was found from the beginning of the test until end of Cycle 7 (the yielding cycle) for Specimens T2, T3 and T4. However, for Specimen T1, the slope was calculated from the beginning of the test until Cycle 1,001 (yielding cycle for wind protocol), and then multiplying the rotational stiffness by the base moment (M_{base}) at each corresponding step of the test for all specimens. The rotational spring stiffness was calculated as 1.18×10^6 kN-m/rad (0.87×10^6 kip $\cdot$ ft/rad) for Specimen T1, 1.63×10^6 kN-m/rad (1.20×10^6 kip $\cdot$ ft/rad) for Specimen T2,

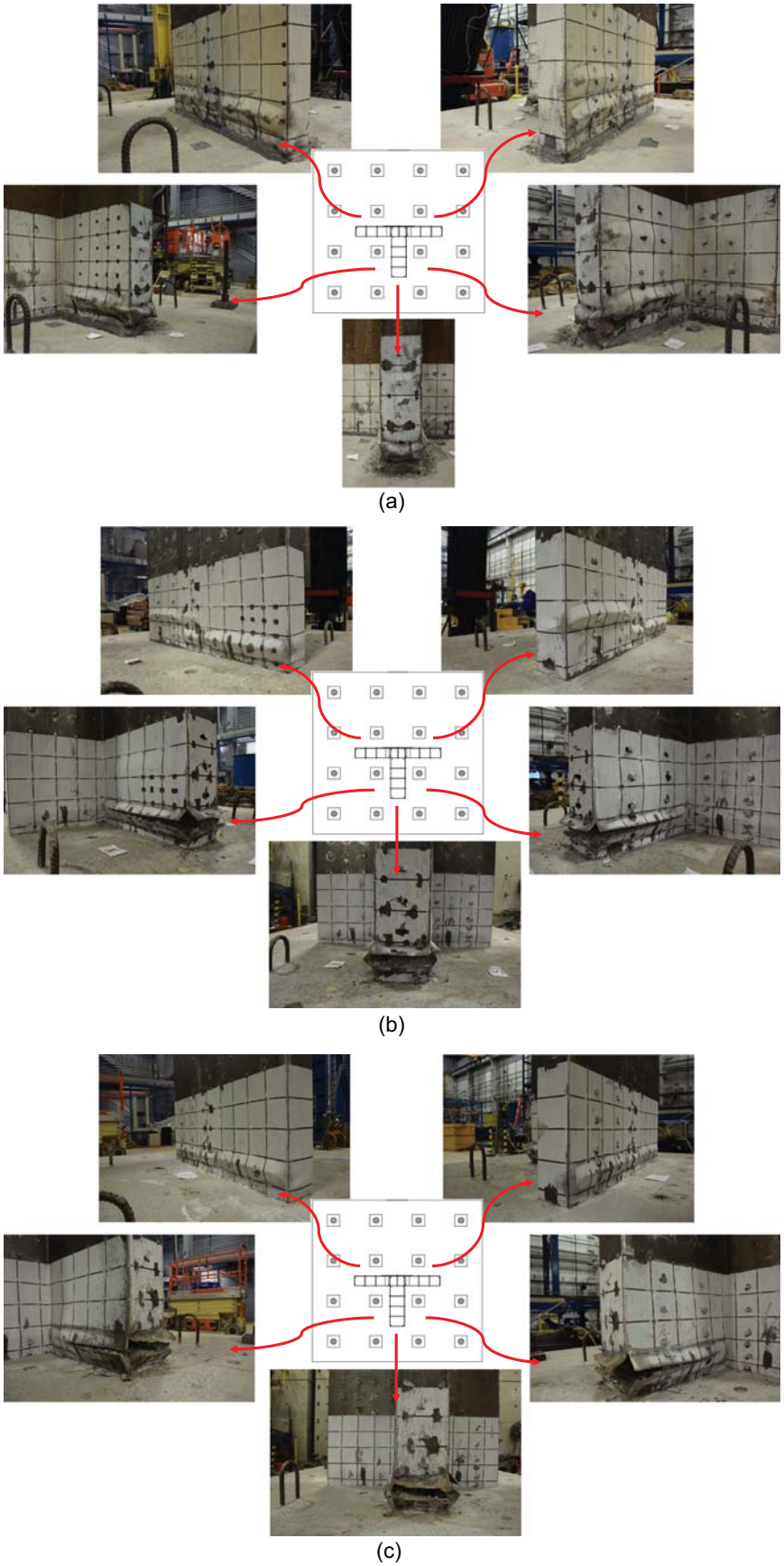

Fig. 14. Post-test damage inspection of the wall steel plates for Specimens (a) T2; (b) T3; and (c) T4.

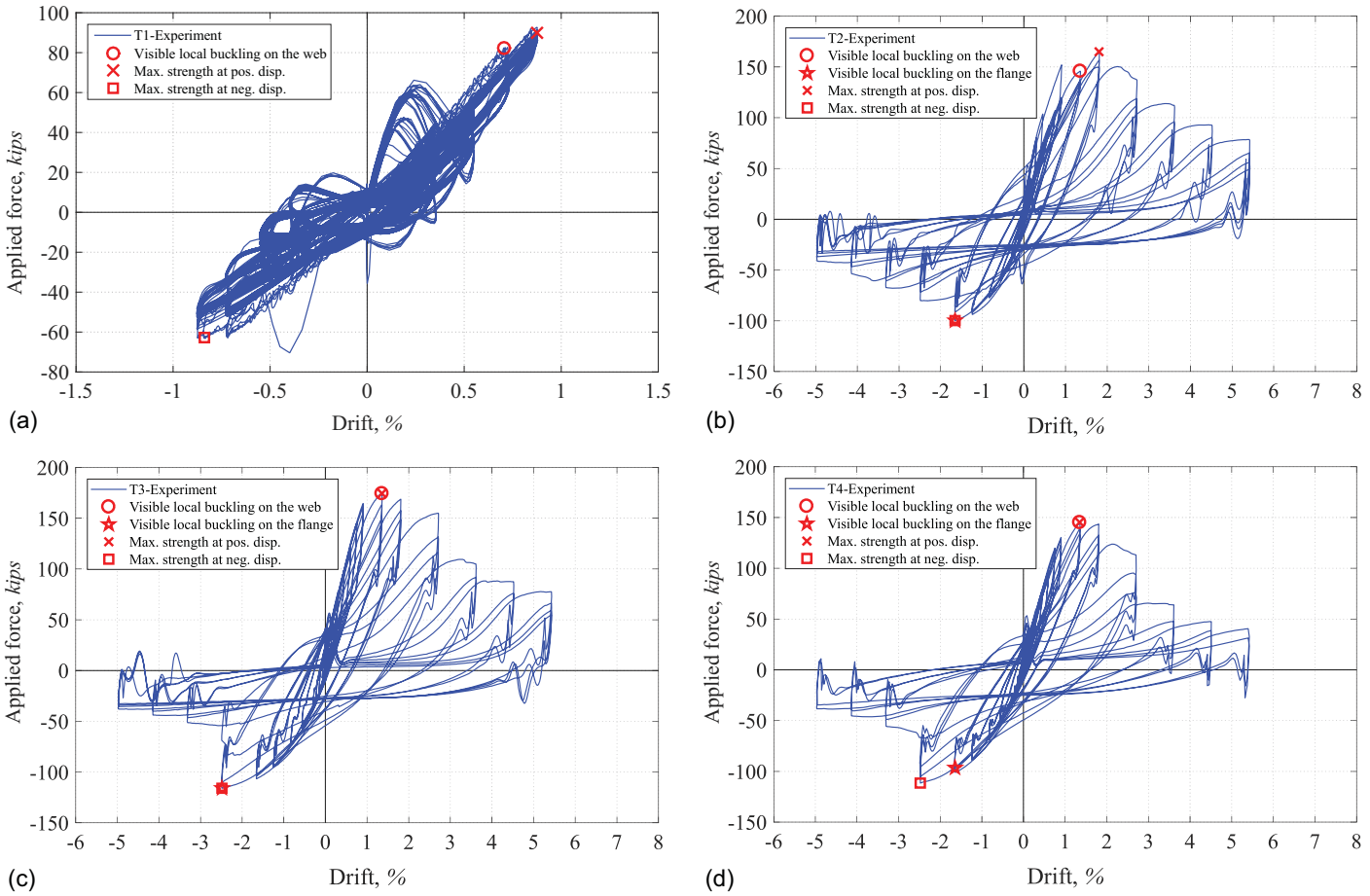

Fig. 15. Applied lateral force versus top drift curves for Specimens (a) T1; (b) T2; (c) T3; and (d) T4; wind loading protocol for T1 and seismic loading protocol for T2, T3, and T4 (1 kip = 1.45 kN).

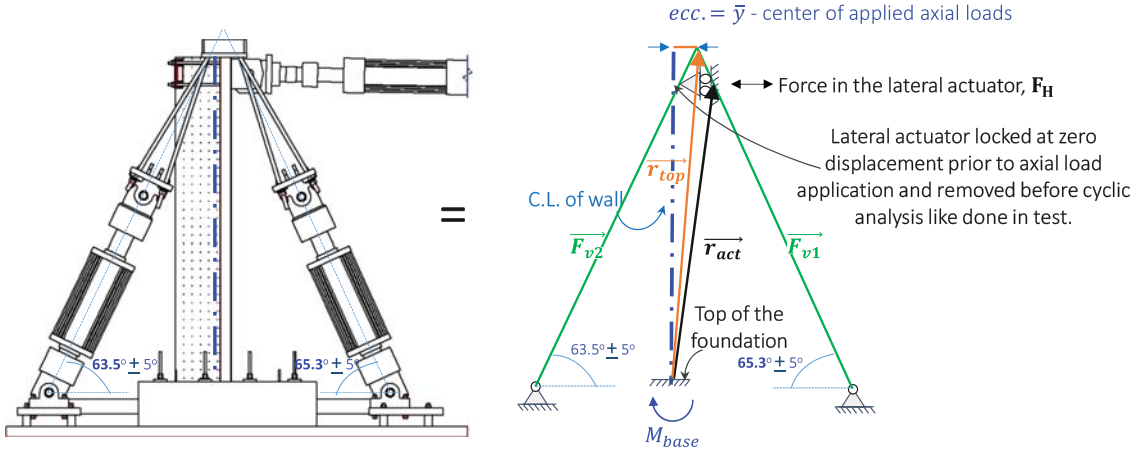

Fig. 16. Inclination angle of vertical actuators at zero displacement and free body diagram of the specimen wall at zero displacement.

1.5×10^6 kN-m/rad (1.10×10^6 kip · ft/rad) for Specimen T3 and 0.79×10^6 kN-m/rad (0.58×10^6 kip · ft/rad) for Specimen T4. Figs. 19(a–d) show the calculated base moment versus the wall rotations (M_{base}-θ_{wb}) relationship curve (blue solid line) with comparison to total rotations at the wall base (M_{base}-θ_{wt}) (black dashed line). Note that Fig. 19(a) is the result from the wind cyclic test protocol, but Figs. 19(b–d) are from the seismic cyclic test protocol.

Comparison between Tests

Normalized moment versus drift plots are used to compare results between various specimens. The moments in both positive and negative directions were normalized with their corresponding plastic moment values considering the axial loadings for each specimen. Initial stiffness, maximum strength, drift at which maximum strength is reached, and strength deterioration after peak are compared.

Table 6. Actual, nominal, and expected material properties and calculated flexural resistances for all specimens

Specimen	Material property	Concrete f'_c, ksi	Steel plates F_y, ksi	M_y, kip-ft				M_{PSDM}, kip-ft				$\frac{M_{PSD}}{M_y}$		$\frac{M_{exeriment}}{M_{PSDM}}$	
				Pos.	y_{NA}, in.	Neg.	y_{NA}, in.	Pos.	y_{NA}, in.	Neg.	y_{NA}, in.	Pos.	Neg.	Pos.	Neg.
T1	Nominal	6.0	50.0	1,042	10.26	648	7.67	1,904	9.26	1,198	3.24	1.83	1.85	0.62	0.88
	Actual	3.6	54.0	877	8.77	680	8.48	1,561	6.16	1,220	4.61	1.78	1.79	0.76	0.87
	Expected	7.65	55.0	1,400	11.40	742	6.94	2,222	11.17	1,318	2.87	1.59	1.78	0.54	0.80
T2	Nominal	6.0	50.0	935	4.86	938	10.15	1,810	6.11	1,433	4.66	1.94	1.53	1.17	1.09
	Actual	5.7	54.0	1,035	5.44	924	10.37	1,823	6.05	1,495	4.89	1.76	1.62	1.16	1.05
	Expected	7.65	55.0	1,291	7.44	970	9.38	2,210	6.39	1,573	4.01	1.71	1.62	0.96	0.99
T3	Nominal	6.0	50.0	935	4.83	942	10.17	1,810	6.11	1,434	4.66	1.94	1.53	1.14	1.42
	Actual	6.06	61.07	1,290	6.82	1,012	9.80	2,015	6.09	1,639	4.84	1.56	1.62	1.02	1.24
	Expected	7.65	55.0	1,317	7.42	971	9.39	2,210	6.39	1,575	4.02	1.68	1.62	0.93	1.29
T4	Nominal	6.0	50.0	1,033	7.21	806	9.50	1,860	6.28	1,354	4.14	1.8	1.68	0.96	1.34
	Actual	4.17	60.03	992	9.41	908	9.81	1,688	5.94	1,468	5.39	1.70	1.62	1.06	1.24
	Expected	7.65	55.0	1,350	9.11	908	8.41	2,240	8.01	1,486	3.60	1.66	1.64	0.8	1.22

Note: y_{NA} is the location of the neutral axis from the face of flange. 1 in. = 25.4 mm; 1 ksi = 6.9 MPa; 1 kip-ft = 1.36 kN-m. Pos. = positive; and Neg. = negative.

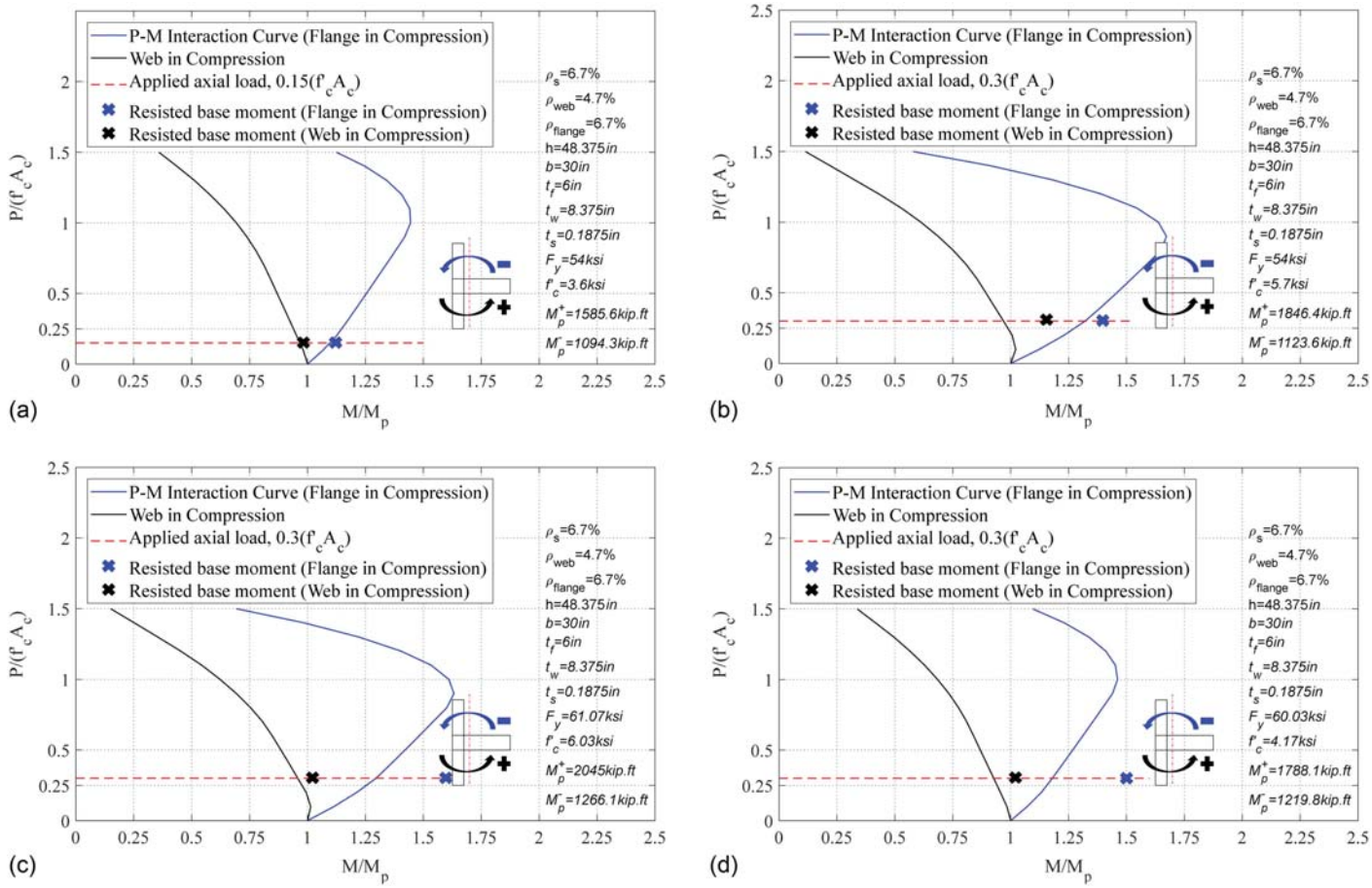

Fig. 17. Comparison of Specimens (a) T1; (b) T2; (c) T3; and (d) T4 flexural resistances with P-M interaction curve (1 in. = 25.4 mm; 1 ksi = 6.9 MPa; and 1 kip-ft = 1.36 kN-m).

Given that the T-shaped wall was designed to correspond to half of the C-shaped wall, Fig. 20 shows this comparison between Specimens C1 [from Kenarangi et al. (2020, 2021) test series] and T2. Despite the fact that the loading protocols were not the same, and that axial loading applied to the specimens were not exactly the same (19% and 30% of $A_c f'_c$ for Specimens C1 and T2, respectively). It is observed that the initial stiffness in the positive direction is almost the same, and that the initial stiffness of Specimen T2 in the negative direction is 28.8% higher than that of Specimen C1. It is also observed that the maximum positive and negative strengths occurred at almost the same drifts. However, the maximum strength of Specimen T2 is $7.8\%/-5.6\%$ higher

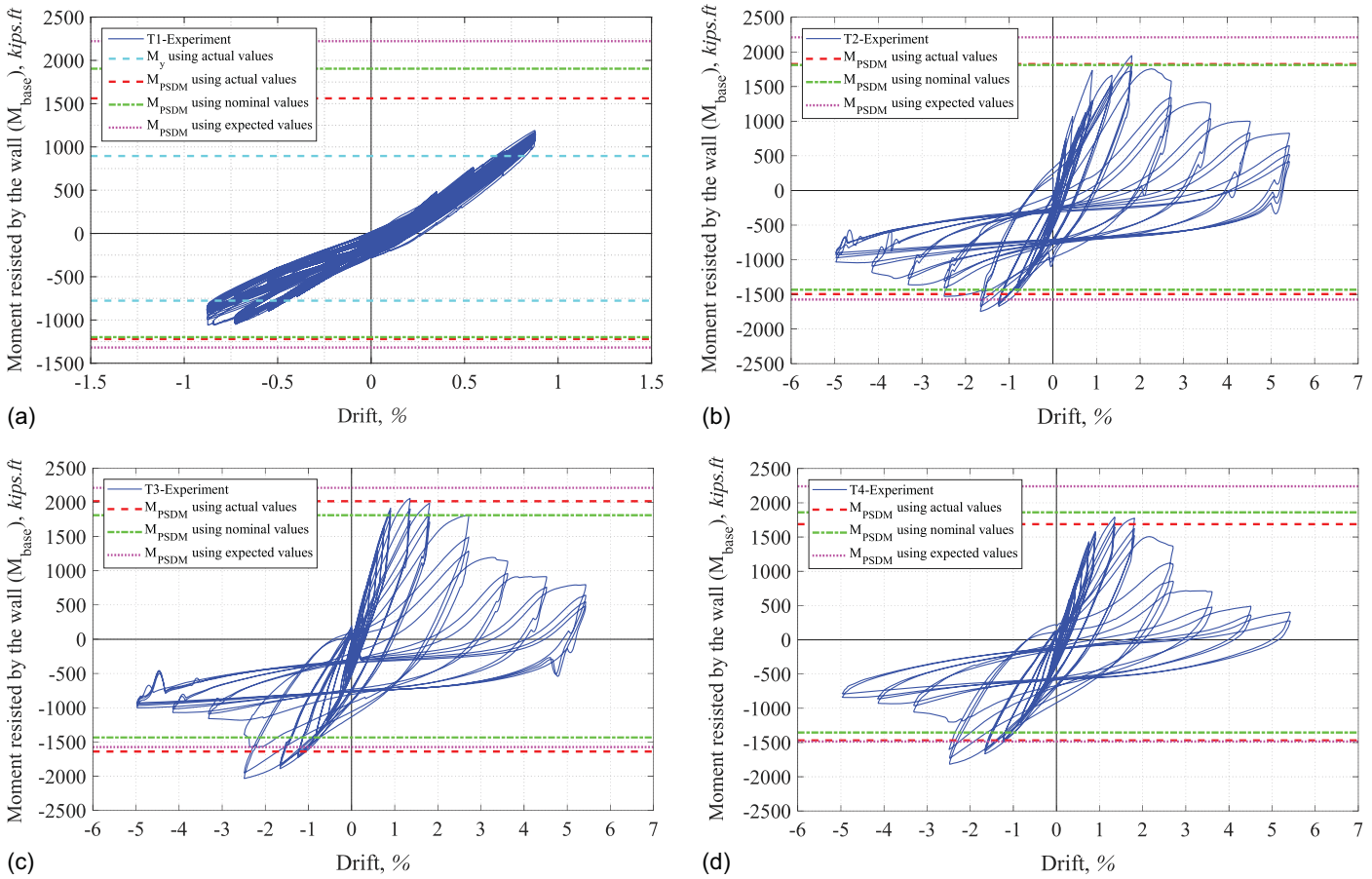

Fig. 18. Comparison of calculated theoretical resistance moments and the experimental base moment for Specimens (a) T1; (b) T2; (c) T3; and (d) T4; wind loading protocol for T1 and seismic loading protocol for T2, T3, and T4 (1 kip-ft = 1.36 kN-m).

than Specimen C1 [excluding the peak of Specimen C1 in the positive direction for reasons explained in Kenarangi et al. (2020, 2021)] in the positive and in the negative directions, respectively. The strength degradations in both directions are also close to each other after the peak. Note that both specimens had the same tie bar spacing and tie bar diameter.

Fig. 21 shows the comparison between Specimens T2 and T3. The only difference between these two specimens is the spacing of tie bars, namely 152.4 mm (6 in.) spacing for Specimen T2 and 114.3 mm (4.5 in.) spacing for Specimen T3. Both specimens had the same tie bar diameter. The initial stiffness of Specimen T3 in the positive direction is 23.1% higher than that of Specimen T2, and vice-versa in the negative direction (37.5% higher). The maximum strengths of Specimen T3 are 0.4%/ − 3.6% higher than Specimen T2 in positive and negative directions, respectively. However, the drifts at which maximum strengths were reached is different. The maximum positive strengths were reached at 1.81% and 1.35% drifts in Specimens T2 and T3, respectively, which is relatively close. Alternatively, drifts at which maximum negative strengths occurred are 1.66% and 2.49% for Specimens T2 and T3, respectively. Moreover, the strength degradation after peaks are close to each other in the positive drift direction. However, fracture propagation in the negative direction was rather rapid and sudden after maximum strength in Specimen T3, and it lost almost 40% of its maximum strength in the next cycle. This indicates that the specimen with shorter tie bar spacing experienced more rapid fracture and sudden strength degradation.

Fig. 22 shows the comparison between Specimens T3 and T4. Both specimens had the same tie bar spacing [114.3 mm (4.5 in.)] but different tie bar diameter (12.7 mm (0.5 in.) for Specimen T3 and 6.4 mm (0.25 in.) for Specimen T4). The initial stiffnesses in both directions are effectively the same for both specimens. The maximum strengths in the positive direction are the same but Specimen T4 had a 5.7% higher strength in the negative direction. However, both maximum positive and negative strengths occurred at the same drift (1.35%/ − 2.49%). The fracture propagation in Specimen T4 was relatively more rapid in the positive direction. This is because more of the welds around tie bars fractured compared to other tests, which suggests that this might have been avoidable if the fillet welds to the ties had not been ground (as mentioned earlier). However, in the negative direction, the propagation of fracture during testing of Specimen T4 was slightly less severe than for Specimen T3, and there was also a slight increase in the maximum strength in the negative direction, although this may be coincidental and not necessarily attributable to the reduction in tie bar size.

Finally, comparing the number of failures at the welds connecting the tie bars to the wall plates, the welds around five tie bars failed between cycles 23 to 25 in Specimen T3, compared to eleven tie bars welds between cycles 21 to 24 in Specimen T4 (Kizilarslan et al. 2021). While this is a significant difference, it remains inconclusive here due to the fact that the tie bars and their weld were significantly ground off during their fabrication, contrary to what had been specified, and this could have detrimentally affected the strength of the fillet welds as described earlier. Nonetheless, to investigate this further, some photos were taken of the tie bars after the walls were cut from their base for disposal. It was observed that some of the 6.4 mm (0.25 in.) tie bars from Specimen T4

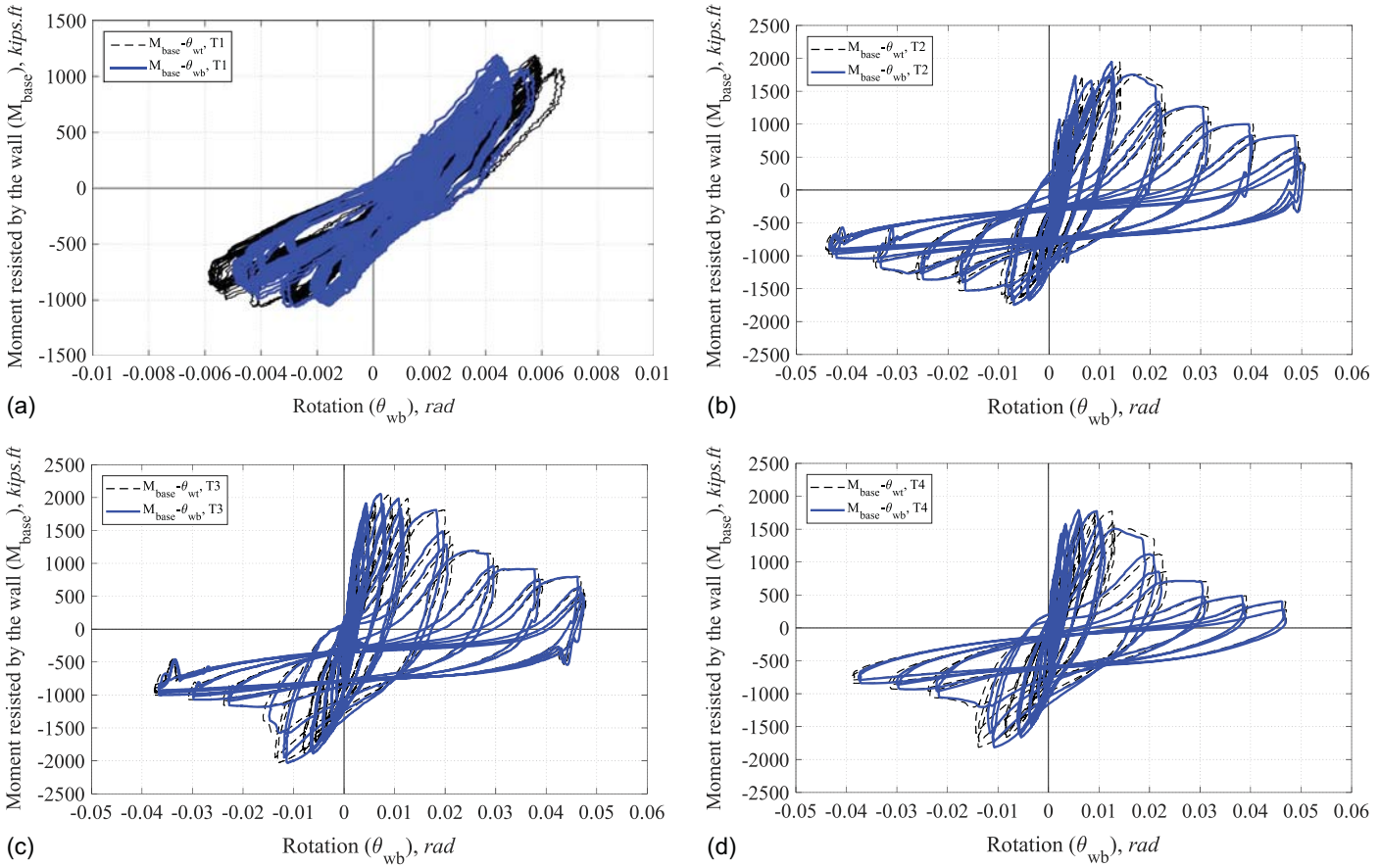

Fig. 19. Comparison of calculated experimental base moment versus wall base rotation and versus total base rotation for Specimens (a) T1; (b) T2; (c) T3; and (d) T4; wind loading protocol for T1 and seismic loading protocol for T2, T3 and T4 (1 kip-ft = 1.36 kN-m).

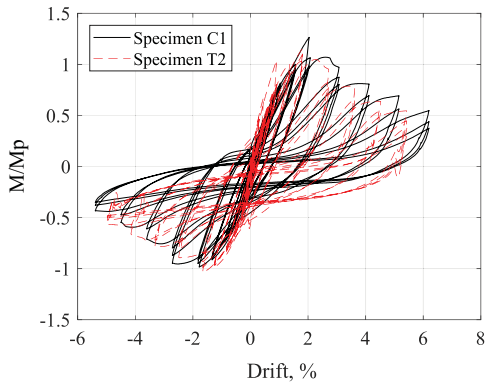

Fig. 20. Comparison between Specimens C1 and T2.

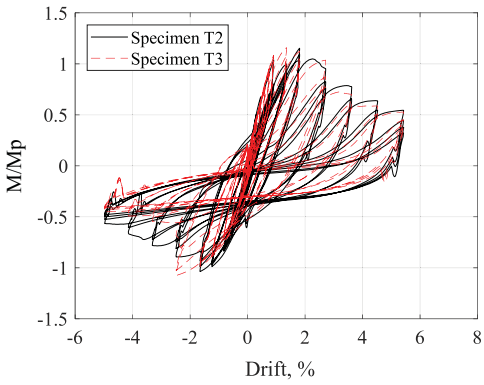

Fig. 21. Comparison between Specimens T2 and T3.

experienced more severe bending, and showed evidence of necking and fracture but that the 12.7 mm (0.5 in.) tie bars only experienced a slight amount of bending and no necking or fracture (Kizilarslan et al. 2021).

Summary and Conclusions

Four large-scale T-shaped composite plate shear wall/concrete filled were subjected to axial and cyclic flexural loading. One of the walls (Specimen T1) was subjected an axial load equal to 15% of the crushing load of concrete (i.e., $A_c f'_c$), and to a wind cyclic loading protocol. For the other three specimens, and axial load equal to 30% of the crushing load of concrete was applied on the specimens and they were cycled with an earthquake cyclic loading protocol.

Specimen T1 had 152.4 mm (6 in.) tie bar spacing and 12.7 mm (0.5 in.) diameter tie bars and it was subjected to 2,120 cycles that ramped up in amplitude from $\pm 0.5\Delta_y$ to $\pm 1.5\Delta_y$ and ramped back down to $\pm 0.5\Delta_y$. Steel plates experienced a slight buckling in the first cycle at $\pm 1.0\Delta_y$ cycle amplitude (i.e., Cycle 1,050) and first fracture was observed during the first cycle at a $\pm 1.5\Delta_y$ cycle amplitude (i.e., Cycle 1,060). At the end of the test, 52% of the web cross section [609.6 mm (24 in.)] remained unfractured.

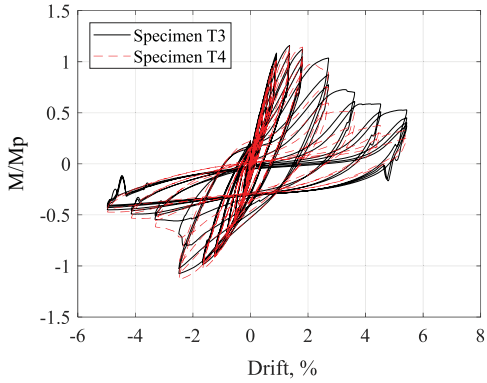

Fig. 22. Comparison between Specimens T3 and T4.

The force-displacement curves obtained from the test were almost linear with little energy dissipation. However, the specimen exceeded its calculated yield moment capacities using actual material strengths in both positive and negative loading directions.

Fabrication flaws in the CJP welds between the wall's steel plates and thicker plates embedded inside of the footing of Specimens T1 and T2 induced premature fractures at points that were not intended to be part of the failure mechanics, which led to a reduced cyclic performance for these two tested specimens. Therefore, Specimens T3 and T4 were fabricated with doubler plate details and better quality control, and tested to determine the true cyclic inelastic behavior of T-shaped walls in absence of flaws. As expected for such composite structures, the hysteretic behavior of walls T3 and T4 started to degrade when fracture was triggering at the apex of the local buckles due to low cycle fatigue upon repeated cycles of inelastic buckling.

Note that Specimen T2 had 152.4 mm (6 in.) tie bar spacing with 12.7 mm (0.5 in.) tie bar diameter, in compliance with the detailing requirements of AISC-341 (AISC 2016) Clause H7. Specimens T3 and T4 both had the tighter 114.3 mm (4.5 in.) tie bar spacing required by ASCE-7 (ASCE 2022) [and forthcoming in AISC–341 (AISC 2022) Clauses H8 and updated H7], but with different tie bar diameters of 12.7 mm (0.5 in.) and 6.4 mm (0.25 in.), respectively. In the first case, bar diameter was calculated per the earlier AISC-341 (AISC 2016) Clause H7 requirements; in the second case, tie diameter was determined per the requirements of ASCE 7 (ASCE 2022) [and forthcoming in AISC-341 (AISC 2022) Clauses H8 and updated H7].

The ductility obtained from these tests was $2.13/-3.23$, $3.07/-2.77$, and $2.29/-2.60$ for Specimens T2, T3, and T4, respectively, in the positive and negative loading directions, with peak ductility calculated at the point when flexural strength dropped to 80% of the peak value developed. Moreover, all specimens reached or exceeded their calculated plastic moment capacities in the positive and negative direction. More specifically:

- Peak strength was reached at drifts of $1.81\%/-1.66\%$ for Specimen T2. In comparison, the peak strengths were observed at $1.35\%/-2.49\%$ drifts for Specimens T3 and T4.
- Tests showed that even though local buckling started in early cycles after yielding, the capacity of the walls did not drop until fracture of the steel plates.
- The fracture propagation of steel plates was more rapid for the Specimens that had closer spacing of tie bars. For Specimen T2 which had 152.4 mm (6 in.) tie bar spacing, it was relatively more progressive than for Specimens T3 and T4 [114.3 mm (4.5 in.) tie bar spacing], and Specimen T2 consequently exhibited a relatively slower flexural strength degradation. The maximum strength drop observed in Specimen T2 is 14.4% between -1.66% and -2.5% drifts (after maximum strength) and it is 12.4% between -2.5% and -3.32%. However, it is 49.4% between -2.5% and -3.32% drifts for Specimens T3 and T4 after maximum strength.
- A significant portion of web and flange remained unfractured at peak drifts of $5.4/-5.0\%$ when testing was stopped, and a residual flexural strength of $27.9/-46.1\%$, $29.1/-37.7\%$, and $21.6/-38.4\%$ of corresponding peak values remained for Specimens T2, T3, and T4 in the positive and negative directions, respectively, at these drifts (i.e., at completion of the tests).
- The maximum rotations when flexural strength dropped to 80% of the peak value developed were $0.021/-0.022$, $0.022/-0.016$, $0.015/-0.015$ for Specimens T2, T3, and T4, respectively. The maximum rotation in the positive direction of Specimen T3 was larger than the others. In the positive direction, the maximum rotations of Specimens T2 and T3 are almost the same, and Specimen T4 had a smaller rotation. In the negative direction, the maximum rotation of Specimen T2 was higher than for Specimens T3 and T4 that exhibited the same maximum base rotation in the negative direction. Overall, Specimen T4, with smaller tie bar diameters, was the one that developed the smaller maximum rotations.
- Yielding propagated over roughly 35%–50% of the height of the wall, given that the ratio of plastic moment to first yield moment was in the range of 1.53 to 1.94 (depending on direction of loading) when strengths were calculated based on the actual steel and concrete material strengths (from coupons and cylinder tests). As a result, buckling occurred between a few layers of tie bars, but yielding spread over a substantial part of the wall height.

Based on the experimental observations and results obtained, it can be concluded that T-shaped C–PSW/CF can exhibit good cyclic behavior without strength degradation for drift ratio less than 2%, while maintaining their ability to resist large axial load of up to 30% $A_c f'_c$.

Data Availability Statement

Some or all data, models, or code that support the findings of this study are available from the corresponding author upon reasonable request.

Acknowledgments

This research was performed with support from the Charles Pankow Foundation (CPF) and the American Institute of Steel Construction (AISC), through CPF research Grant #06-16 awarded to co-PIs Michel Bruneau, from University at Buffalo and Amit H. Varma, from Purdue University. This paper focuses on a part of the work conducted at the University at Buffalo only. The researchers also thank Magnusson Klemencic Associates (MKA), Cives Steel Co., J. F. Stearns Co., and Turner Construction, for donating steel and fabrication of specimens tested. The authors also thank members of the Project Advisory Team (Ron Klemencic, Chairman and CEO, MKA; Larry Kruth, Vice President, American Institute of Steel Construction (AISC); Jim Malley, Senior Principal, Degenkolb Engineers; Ron Hamburger, Senior Principal at SGH; Devin Huber, Director of Research, AISC) for their valuable technical guidance. All opinions, findings, conclusions, and recommendations presented in this paper are those of the authors and do not necessarily reflect the view of the sponsors.

Supplemental Materials

Figs. S1 and S2 are available online in the ASCE Library (www.ascelibrary.org).

References

Abdullah, S., K. Aswegan, R. Klemencic, and J. Wallace. 2020. *Experimental study of concrete coupling beams subjected to wind and seismic loading protocols*. Rep. No. UCLA SEERL 2020 1. Los Angeles: Univ. of California.

Adams, P. F., T. J. E. Zimmerman, and J. G. MacGregor. 1987. "Design and behavior of composite ice-resisting walls." In *Proc., Port and Ocean Engineering Under Arctic Conditions*, 663–674. Fairbanks, AK: Port and Ocean Engineering Under Artic Condition.

AISC. 2014. *Specification for safety-related steel structures for nuclear facilities, supplement No. 1*. AISC-N690. Chicago: AISC.

AISC. 2016. *Seismic provisions for structural steel buildings*. AISC-341-16. Chicago: AISC.

AISC. 2022. *Seismic provisions for structural steel buildings*. AISC-341-22. Chicago: AISC.

Akita, S., M. Ozaki, N. Niwa, I. Matsuo, and K. Hara. 2001. "Study on steel plate reinforced concrete bearing wall for nuclear power plants Part 2; analytical method to evalute response of SC walls." In *Proc., Transactions of the 6th Int. Conf. on Structural Mechanics in Reactor Technology.* Washington, DC: SMIRT 16.

Akiyama, H., H. Sekimoto, M. Tanaka, K. Inoue, M. Fukihara, and Y. Okuda. 1989. "1/10th scale model test of inner concrete structure composed of concrete filled steel bearing wall." In *Proc., Transactions of the 10th Int. Conf. on Structural Mechanics in Reactor Technology.* Washington, DC: DOE.

Alzeni, Y., and M. Bruneau. 2014. *Cyclic inelastic behavior of concrete filled sandwich panel walls subjected to in-plane flexure*. Technical Rep. No. MCEER 14-009. Buffalo, NY: State Univ. of New York at Buffalo.

Alzeni, Y., and M. Bruneau. 2017. "In-plane cyclic testing of concrete-filled sandwich steel panel walls with and without boundary elements." *J. Struct. Eng.* 143 (9): 04017115. https://doi.org/10.1061/(ASCE)ST.1943-541X.0001791.

ASCE. 2019. *Prestandard for performance-based wind design*. Reston, VA: ASCE.

ASCE. 2022. *Minimum design loads for buildings and other structures*. ASCE-7. Reston, VA: ASCE.

ATC (Applied Technology Council). 1992. *Guidelines for cyclic seismic testing of components of steel structures*. ATC-24. Richmond, VA: ATC.

Bhardwaj, S. R., and A. H. Varma. 2017. *Design of modular steel-plate composite walls for safety related nuclear facilities*. Chicago: AISC.

Bowerman, H., and J. C. Chapman. 2002. "Bi-steel steel-concrete-steel sandwich construction." In *Proc., Composite Construction in Steel and Concrete IV*, 656–667. Reston, VA: ASCE.

Bowerman, H., M. Gough, and C. King. 1999. *Bi-Steel design and construction guide*. Scunthorpe, UK: British Steel Ltd.

Bruhl, J. C., and A. H. Varma. 2018. "Experimental evaluation of steel-plate composite walls subject to blast loads." *J. Struct. Eng.* 144 (9): 04018155. https://doi.org/10.1061/(ASCE)ST.1943-541X.0002163.

Eom, T.-S., H.-G. Park, C.-H. Lee, J.-H. Kim, and I.-H. Chang. 2009. "Behavior of double skin composite wall subjected to in-plane cyclic loading." *J. Struct. Eng.* 135 (10): 1239–1249. https://doi.org/10.1061/(ASCE)ST.1943-541X.0000057.

Epackachi, S., N. H. Nguyen, E. G. Kurt, A. S. Whittaker, and A. H. Varma. 2015. "In-plane seismic behavior of rectangular steel-plate composite wall piers." *J. Struct. Eng.* 141 (7): 04014176. https://doi.org/10.1061/(ASCE)ST.1943-541X.0001148.

Gerwick, B., and D. Berner. 1987. "Utilization of composite design in the arctic and sub-arctic." In *Proc., Port and Ocean Engineering Under Arctic Conditions*, 663–674. Fairbanks, AK: Port and Ocean Engineering Under Artic Condition.

JEA (Japanese Electric Association). 2005. *Technical guidelines for seismic design of steel plate reinforced concrete structures: Buildings and structures*. JEAG 4618. Tokyo: JEA.

Kenarangi, H., E. Kizilarslan, and M. Bruneau. 2020. *Cyclic inelastic behavior of C-shaped composite plate shear walls-concrete filled (C-PSW/CF) walls*. Charles Pankow Foundation Grant # 06-17. McLEan, VA: Charles Pankow Foundation.

Kenarangi, H., E. Kizilarslan, and M. Bruneau. 2021. "Cyclic behavior of c-shaped composite plate shear walls–concrete filled." *Eng. Struct.* 226 (Jan): 111306. https://doi.org/10.1016/j.engstruct.2020.111306.

Kizilarslan, E. 2021. "Experimental and analytical inelastic behavior of C- and T-shaped composite plate shear walls/concrete-filled (C-PSW/CF)." Ph.D. dissertation, Dept. of Civil, Structural and Environmental Engineering, State Univ. of New York at Buffalo.

Kizilarslan, E., and M. Bruneau. 2021. "Hysteretic response of repaired C-shaped concrete filled composite plate shear walls (CF-CPSWs)." *Eng. Struct.* 241 (Aug): 112410. https://doi.org/10.1016/j.engstruct.2021.112410.

Kizilarslan, E., H. Kenarangi, and M. Bruneau. 2021. *Cyclic inelastic behavior of T-shaped composite plate shear walls-concrete filled (C-PSW/CF) walls*. Charles Pankow Foundation Grant # 06-17. McLEan, VA: Charles Pankow Foundation.

Liew, J. R., and T. Wang. 2011. "Novel steel-concrete-steel sandwich composite plates subject to impact and blast load." *Adv. Struct. Eng.* 14 (4): 673–687. https://doi.org/10.1260/1369-4332.14.4.673.

Matsuishi, M., and S. Iwata. 1987. "Strength of composite, sandwich system, ice-resisting structures." In *Proc., Port and Ocean Engineering under Arctic Conditions*, 689–698. Fairbanks, AK: Port and Ocean Engineering Under Artic Condition.

O'Flynn, B., and J. MacGregor. 1988. *Tests on composite ice-resisting walls*, 699–710. Fairbanks, AK: Univ. of Alaska Fairbanks.

Ozaki, M., S. Akita, H. Osuga, T. Nakayama, and N. Adachi. 2004. "Study on steel plate reinforced concrete panels subjected to cyclic in-plane shear." *Nucl. Eng. Des.* 228 (1–3): 225–244. https://doi.org/10.1016/j.nucengdes.2003.06.010.

Ramesh, S. 2013. *Behavior and design of earthquake-resistant dual-plate composite shear wall systems*. West Lafayette, IN: Purdue Univ.

Sasaki, N., H. Akiyama, M. Narikawa, K. Hara, M. Takeuchi, and S. Usami. 1995. "Study on a concrete filled steel structure for nuclear power plants (Part 3). Shear and bending loading tests on wall member." In *Proc., Transactions of the 13th Int. Conf. on Structural Mechanics in Reactor Technology.* Porto Alegre, Brazil: SMIRT 13.

Shafaei, S. 2020. "Seismic and wind behavior of planar composite plate shear walls concrete filled (C PSWCF)." Ph.D. dissertation, Lyles School of Civil Engineering, Purdue Univ. Graduate School.

Shafaei, S., A. H. Varma, J. Seo, and R. Klemencic. 2021. "Cyclic lateral loading behavior of composite plate shear walls/concrete filled." *J. Struct. Eng.* 147 (10): 04021145. https://doi.org/10.1061/(ASCE)ST.1943-541X.0003091.

Smith, J., and A. McLeish. 1987. "The resistance of composite steel/concrete structures to localized ice loading." In *Proc., Port and Ocean Engineering under Arctic Conditions*, 675–687. Fairbanks, AK: Port and Ocean Engineering Under Artic Condition.

Takeuchi, M., H. Akiyama, M. Narikawa, K. Hara, H. Tsubota, and I. Matsuo. 1995. "Study on a concrete filled steel structure for nuclear power plants (Part 1). Outline of the structure and the mock-up test." In *Proc., Transactions of the 13th Int. Conf. on Structural Mechanics in Reactor Technology.* Porto Alegre, Brazil: SMIRT 13.

Varma, A. H., S. R. Malushte, K. C. Sener, and Z. Lai. 2014. "Steel-plate composite (SC) walls for safety related nuclear facilities: Design for in-plane forces and out-of-plane moments." *Nucl. Eng. Des.* 269 (Apr): 240–249. https://doi.org/10.1016/j.nucengdes.2013.09.019.

Wright, H. 1998. "Axial and bending behavior of composite walls." *J. Struct. Eng.* 124 (7): 758–764. https://doi.org/10.1061/(ASCE)0733-9445(1998)124:7(758).